J. Fluid Mech. (2007), *vol.* 572, *pp.* 471–504. © 2007 Cambridge University Press
doi:10.1017/S0022112006001893 Printed in the United Kingdom

Leading-edge effects in bypass transition

By S. NAGARAJAN, S. K. LELE AND J. H. FERZIGER†
Department of Mechanical Engineering, Stanford University, Stanford, CA 94305, USA

(Received 21 January 2005 and in revised form 14 March 2006)

The effect of a blunt leading edge on bypass transition is studied by numerical simulation. A mixed direct and large-eddy simulation of a flat plate with a super-ellipse leading edge is carried out at various conditions. Onset and completion of transition is seen to move upstream with increasing bluntness. For sharper leading edges, at lower levels of turbulence, transition usually occurs through instabilities on low-speed streaks as observed by Jacobs & Durbin (2001) and Brandt *et al.* (2004) whereas increasing either the turbulence intensity or the leading-edge bluntness brings into play another mechanism. Free-stream vortices are amplified at the leading edge because of stretching. In the case of particularly strong vortices, this interaction induces a localized streamwise vortical disturbance in the boundary layer which then grows as it convects downstream and eventually breaks down to form a turbulent spot. These disturbances, which are localized and hence wavepacket-like, move at speeds in the range $0.55U_\infty$–$0.65U_\infty$ and occur in the lower portion of the boundary layer. Simulations conducted with isolated vortices confirm such a response of the boundary layer.

1. Introduction

1.1. *Bypass transition in a flat-plate boundary layer*

In the presence of free-stream turbulence (FST), boundary layer transition does not follow the mechanism of growth of Tollmien–Schlichting (TS) waves followed by three-dimensional modulation and breakdown to turbulence, a process that is commonly referred to as *natural transition*. Instead, transition occurs sooner, via mechanisms not yet fully understood. Morkovin (1969) called this *bypass transition*, a term indicative of the fact that the aforementioned natural transition path to turbulence is bypassed. This process is characterized by growth over time scales much shorter than the viscous scale of TS waves. As a result, boundary layer transition can occur at momentum-thickness Reynolds numbers (Re_θ) of the few hundred instead of the few thousand that is typical of natural transition.

There have been many experimental, computational, and analytical studies of bypass transition, but the path to turbulence under a broad range of conditions remains a mystery. Dryden (1936), conducting experiments on boundary layers observed that "the Reynolds number at which transition occurs is a function of the initial turbulence of the air stream, decreasing as the turbulence is increased" and also that "the laminar and eddying regions cannot be distinguished on the basis of the magnitude of the speed fluctuation", now well-recognized aspects of boundary layers forced by FST. In their experiments, Klebanoff, Tidstrom & Sargent (1962) also

† Professor Joel H. Ferziger passed away on August 16, 2004 while this paper was being written.

https://doi.org/10.1017/S0022112006001893 Published online by Cambridge University Press

observed large spanwise variations in streamwise velocity, which were subsequently named Klebanoff modes or K-modes by Kendall (1985). These are not modes in the strict sense, i.e. they are not solutions to an eigenvalue problem. Klebanoff modes are usually depicted in terms of RMS profiles of fluctuating streamwise velocity inside the boundary layer. Experiments have shown the fluctuations to be large, reaching up to 20 % of the mean free-stream velocity. However, in spite of such high levels of disturbance, the mean velocity profile in the boundary layer prior to transition remains unchanged (Westin *et al.* 1994).

It is believed that Klebanoff modes are somehow responsible for transition, and a lot of experimental effort has gone into observing these modes (Roach & Brierley 1992; Westin *et al.* 1994; Matsubara & Alfredsson 2001). These experiments show that while the fluctuation level outside the boundary layer decays downstream, fluctuations in streamwise velocity inside the boundary layer increase, with the peak in the RMS fluctuation around the middle of the boundary layer. Furthermore, frequency spectra inside the boundary layer show a marked shift toward lower frequencies, indicating that higher frequencies in the FST do not penetrate into the boundary layer, a phenomenon called shear sheltering (Jacobs & Durbin 1998; Hunt & Durbin 1999). The spanwise correlation of the streamwise velocity perturbation u' shows a strong anti-correlation at separations of the order of the boundary layer thickness. From these observations, it is clear that the dominant modes in the boundary layer are streamwise elongated streaky structures with a spanwise scale of the order of the boundary layer thickness. However, the connection between Klebanoff modes and transition remains uncertain as the RMS fluctuations and averaged spectra do not provide any inkling of how transition actually occurs.

The formation of boundary layer structures with spanwise variation in streamwise velocity has been analysed using the theory of optimal disturbances (Andersson, Berggren & Henningson 1999; Luchini 2000). This is based on the theory of transient growth of disturbances, a result of the non-self-adjoint (and non-normal) governing equations (Butler & Farrell 1992; Trefethen *et al.* 1993; Reddy & Henningson 1993). Although exponentially growing modes dominate over long time, algebraic growth can be significant in the transient, overwhelming the eigenmodes in their initial stages of growth. In fact, algebraic growth can occur even when all the eigenmodes are decaying. The linear analyses of Andersson *et al.* (1999) and Luchini (2000) indicate that the flow structure that can cause the largest transient growth at a particular streamwise distance L from the leading edge is a pair of counter-rotating streamwise vortices with a spanwise separation of $1.4\delta_L$, where δ_L is the boundary layer thickness at $x = L$. Downstream of L, i.e. for $x > L$, the disturbance decays due to the effect of spanwise ellipticity, i.e. the effect of spanwise viscous terms in the governing equations. In more recent work, Zaki & Durbin (2005) consider the effect of oblique modes on bypass transition. They show, using the Orr–Sommerfeld and Squire equations and the continuous spectra of both operators, that for certain mean flow profiles, both have the same dispersion relation. They conclude that streaks are formed as a result of secular growth due to resonant forcing of Squire's modes by the corresponding Orr–Sommerfeld continuous mode (Hultgren & Gustavsson 1981; Benney & Gustavsson 1981). Transition occurs when streaks are perturbed by higher frequency modes in the free stream. They were able to reproduce the formation of turbulent spots with only two continuous modes specified at the inlet of their computational domain.

This transition mechanism was first revealed by the direct numerical simulations (DNS) of Jacobs & Durbin (2001) who observed turbulent spots formed by the interaction of a high-frequency free-stream eddy with a parcel of fluid moving slower

https://doi.org/10.1017/S0022112006001893 Published online by Cambridge University Press

than the mean, which they call *backward jets*. The low-frequency content in the free stream causes the formation of low- and high-speed streaks (Goldstein & Wundrow 1998; Leib, Wundrow & Goldstein 1999; Zaki & Durbin 2005). Turbulent spots are formed due to low-speed streak instability triggered by high-frequency free-stream eddies. Simulations of Andersson *et al.* (2001), Brandt & Henningson (2002), and Brandt *et al.* (2003) focused on secondary instabilities of streaks. They observe sinuous instabilities to be more prevalent that varicose ones, while the streaks become unstable only at very large amplitudes. These instabilities were also observed in the direct simulations of Brandt, Schlatter & Henningson (2004). The backward jet mechanism of Jacobs & Durbin (2001) and the sinuous streak instability seem to be the same mechanism, both centred on a low-speed streak which is distorted asymmetrically, occurring near the edge of the boundary layer.

1.2. *Leading-edge effects*

The transition scenarios discussed in the previous section do not include any of the effects of a leading edge, whose detrimental effects have been recognized by experimentalists. Investigations into the effect of leading-edge bluntness on the boundary layer development were carried out by Kendall (1991) and Watmuff (1997), who observed that changing the aspect ratio of the leading-edge ellipse does not affect the K-mode disturbances in the boundary layer. However, the amplitude of Tollmien–Schlichting waves increases nonlinearly with decreasing aspect ratio. This is to be expected as the receptivity process at the leading edge depends on its geometry. In subsequent experiments, Kendall (1998) observed that free-stream vorticity excited three different kinds of disturbances in the boundary layer. The first were the streaky Klebanoff mode oscillations that have been a hallmark of boundary layers subjected to FST. The second were an outer-layer motion at TS frequencies, and the third, the traditional TS wavepackets which were much lower in amplitude than the other two disturbances. Kendall also observed that the TS wavepackets appear rather sporadically but could not identify the defining feature in the free stream that excites a TS wavepacket.

The transition experiments of Westin *et al.* (1994), and Klingmann *et al.* (1993) used a flat plate with an asymmetric leading edge designed using potential flow simulations to eliminate the adverse pressure gradient region on the leading edge. However, in spite of such a careful design, significant upstream movement of the transition onset location was observed for slightly off-design conditions. Westin *et al.* (1994) attribute this to the peak in the pressure coefficient. The available experimental data suggest that transition moves upstream with increasing leading-edge bluntness.

Of all the bypass transition scenarios presented earlier, only that of Goldstein & Wundrow (1998) considers the effect of the leading edge. They argue that wake-like disturbances that correspond to wall-normal vorticity stretch and tilt around the leading edge to enhance streamwise vorticity in the flow above the flat plate (see figure 1*a*). Their argument is as follows: rapid distortion theory predicts amplification of zero-frequency modes and therefore acts as a low-pass filter. Furthermore, the boundary layer itself selectively amplifies low-frequency, small-spanwise-wavelength disturbances. Therefore, the presence of the leading edge causes selective amplification of low-frequency modes, first by vortex stretching, and then through a low-frequency selection process in the boundary layer. The resulting disturbance is in the form of long streamwise vortices whose effect on the boundary layer was later analysed by Wundrow & Goldstein (2001) using a mixed theoretical–computational approach. They observe that these vortices can cause a wake-like defect in the boundary

https://doi.org/10.1017/S0022112006001893 Published online by Cambridge University Press

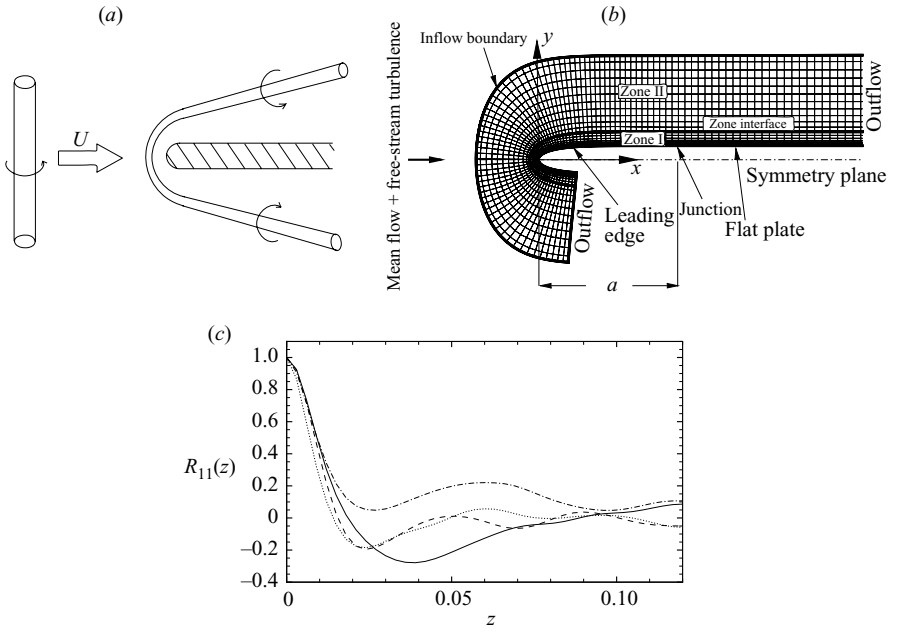


FIGURE 1. (*a*) Effect of leading edge through stretching of vortex tubes. (*b*) Schematic of domain used in simulations of bypass transition (every fourth grid line is shown). The flat plate in the simulations extends further downstream. The origin of the Cartesian system (x, y) is at the nose of the leading edge and the symmetry plane is the stagnation plane for $x < 0$. (*c*) Spanwise correlation of streamwise velocity u inside the boundary layer at different streamwise locations: ——, close to the leading edge; - - - -, just upstream of transition; —·—, in the transition region; · · · ·, in the turbulent boundary layer.

layer profile, similar to the backward jets of Jacobs & Durbin (2001). Formation of turbulent spots is then attributed to growth of inviscid instability waves on the inflectional profile produced.

In summary, even though there is broad agreement that the conditions at the leading edge have significant impact on transition, the additional complexity introduced by the leading edge has been avoided in most theoretical and computational studies of transition. Based on the results available, two possible leading-edge mechanisms have been proposed: (*a*) earlier transition due to better receptivity of blunter leading edges to form TS waves and their increased growth rates in the adverse pressure gradient region, and (*b*) quicker growth of Klebanoff modes due to anisotropy introduced by stretching of vortices around the leading edge, resulting in earlier transition by the same mechanism as when no leading edge is present. One of the goals of this study is to identify the mechanism that leads to transition in the presence of a leading edge and to see if either of the above-mentioned mechanisms is important.

2. The numerical model

2.1. *Governing equations*

The governing equations for three-dimensional unsteady flow of a compressible fluid in a curvilinear coordinate system (x^1, x^2, x^3), written in terms of the contravariant velocity $v^i = \mathrm{d}x^i/\mathrm{d}t$, for a Newtonian fluid obeying Fourier's law of heat conduction

https://doi.org/10.1017/S0022112006001893 Published online by Cambridge University Press

are (see Aris 1989 for a complete derivation)

$$\left.\begin{aligned}
&\frac{d\rho}{dt} + (\rho v^k)_{,k} = 0,\\
&\frac{\partial}{\partial t}(\rho v^i) + (\rho v^i v^j)_{,j} = -(g^{ij}p)_{,j} + \tau^{ij}_{,j},\\
&\frac{\partial E}{\partial t} + [(E+p)v^j]_{,j} = (\kappa g^{ij} T_{,i})_{,j} + (\tau^{ij} g_{ik} v^k)_{,j},
\end{aligned}\right\} \tag{2.1}$$

where density, temperature and pressure are denoted by ρ, T and p respectively, and the total energy E and viscous stress tensor τ^{ij} are given by

$$E = \frac{p}{\gamma - 1} + \tfrac{1}{2}\rho\,|v|^2 = \frac{p}{\gamma - 1} + \tfrac{1}{2}\rho g_{ij} v^i v^j, \tag{2.2}$$

$$\tau^{ij} = \mu\left[g^{jk} v^i_{,k} + g^{ik} v^j_{,k} - \tfrac{2}{3} g^{ij} v^k_{,k}\right]. \tag{2.3}$$

In these equations, the general tensor notation due to Einstein is used (subscripts and superscripts denote covariant and contravariant tensors respectively). g_{ij} and g^{ij} are the covariant and contravariant metric tensors. The subscript, j indicates the covariant derivative, which, for a second-order contravariant tensor A^{ij} may be written as

$$A^{ij}_{,k} = \frac{\partial A^{ij}}{\partial x^k} + \Gamma^i_{pk} A^{pj} + \Gamma^j_{pk} A^{ip} \tag{2.4}$$

where Γ^i_{jk} is the Christoffel symbol of the second kind.

To derive the large-eddy simulation (LES) equations, define a filter $G(\boldsymbol{x})$ with compact support in the domain of interest Ω. Then, any tensor $A^{i_1 \ldots i_m}_{j_1 \ldots j_n}$ may be filtered as

$$\overline{\sqrt{g} A^{i_1 \ldots i_m}_{j_1 \ldots j_n}}(\boldsymbol{x}, t) = \int\!\!\int_{\Omega}\!\!\int A^{i_1 \ldots i_m}_{j_1 \ldots j_n}(\boldsymbol{x}', t) G(\boldsymbol{x} - \boldsymbol{x}') \sqrt{g}\, \mathrm{d}\boldsymbol{x}'. \tag{2.5}$$

The filtered continuity equation suggests that the following curvilinear equivalent of Favre filtering,

$$\widetilde{A}^{i_1 \ldots i_m}_{j_1 \ldots j_n} = \frac{\overline{\sqrt{g}\rho A^{i_1 \ldots i_m}_{j_1 \ldots j_n}}}{\overline{\sqrt{g}\rho}}, \tag{2.6}$$

leaves no unclosed terms in the continuity equation. With this definition, the filtered non-dimensional governing equations become

$$\frac{\partial \overline{\sqrt{g}\rho}}{\partial t} + \frac{\partial}{\partial x^k}(\overline{\sqrt{g}\rho}\ \tilde{v}^k) = 0, \tag{2.7}$$

$$\begin{aligned}
\frac{\partial}{\partial t}(\overline{\sqrt{g}\rho}\,\tilde{v}^i) + \frac{\partial}{\partial x^j}(\overline{\sqrt{g}\rho}\,\tilde{v}^i\tilde{v}^j) + \Gamma^i_{qj}\overline{\sqrt{g}\rho}\,\tilde{v}^q\tilde{v}^j &= -\frac{\partial}{\partial x^j}(g^{ij}\overline{\sqrt{g}\,p}) - \Gamma^i_{qj} g^{qj}\overline{\sqrt{g}\,p}\\
&\quad + \frac{\partial}{\partial x^j}(\overline{\sqrt{g}\tau^{ij}}) + \Gamma^i_{qj}\overline{\sqrt{g}\,\tau^{qj}} - \frac{\partial_{sgs}\tau^{ij}}{\partial x^j} - \Gamma^i_{qj\,sgs}\tau^{qj},
\end{aligned} \tag{2.8}$$

$$\frac{\partial \overline{\sqrt{g}\,E}}{\partial t} + \frac{\partial}{\partial x^j}[\overline{\sqrt{g}(E+p)}\,\tilde{v}^j] = -\frac{\partial}{\partial x^j}(\overline{\sqrt{g}}\tilde{q}^j) + \frac{\partial}{\partial x^j}(\overline{\sqrt{g}\tau^{ij}}\,g_{ik}\,\tilde{v}^k) - \frac{\partial}{\partial x^j}({}_{sgs}q^j), \tag{2.9}$$

https://doi.org/10.1017/S0022112006001893 Published online by Cambridge University Press

where the resolved and subgrid stress tensor and heat flux vector are

$$\tilde{\tau}^{ij} = \frac{\tilde{\mu}}{Re}\left(g^{jk}\tilde{v}^i_{,k} + g^{ik}\tilde{v}^j_{,k} - \tfrac{2}{3}g^{ij}\tilde{v}^k_{,k}\right), \tag{2.10}$$

$$\tilde{q}^j = -\frac{\tilde{\mu}}{RePr}g^{jk}\frac{\partial \widetilde{T}}{\partial x^k}, \tag{2.11}$$

$$_{sgs}\tau^{ij} = \overline{\sqrt{g}\rho}(\widetilde{v^i v^j} - \tilde{v}^i\tilde{v}^j), \tag{2.12}$$

$$_{sgs}q^j = \overline{\sqrt{g}\rho}(\widetilde{T v^j} - \widetilde{T}\tilde{v}^j). \tag{2.13}$$

In addition, the equation of state is

$$\overline{\sqrt{g}p} = \frac{\gamma - 1}{\gamma}\overline{\sqrt{g}\rho}\tilde{T} \tag{2.14}$$

and the expression for pressure in terms of the conserved variables is

$$\overline{\sqrt{g}p} = (\gamma - 1)\left[\overline{\sqrt{g}E} - \tfrac{1}{2}\overline{\sqrt{g}\rho}\, g_{ij}\,\tilde{v}^i\tilde{v}^j - \tfrac{1}{2}\overline{\sqrt{g}\rho}\, g_{ij}(\widetilde{v^i v^j} - \tilde{v}^i\tilde{v}^j)\right]. \tag{2.15}$$

In the derivation of these equations, the metric tensor and Christoffel symbols are assumed to be varying slowly over the spatial support of the filter kernel. They may then be assumed to be constant over the entire filter kernel. In the above equations, physical velocity components are normalized by the free-stream sound speed c_∞, density by the free-stream density ρ_∞, pressure is normalized by $\gamma\rho_\infty c_\infty^2$ and temperature by $(\gamma - 1)T_\infty$.

2.2. *Discretization and simulation conditions*

The governing equations are discretized using a sixth-order compact finite difference scheme on a staggered mesh (Nagarajan *et al.* 2003). Time marching is through a fully implicit, second-order-accurate Beam–Warming scheme in the region near the body, and a third-order Runge–Kutta scheme in the region away from the body (Nagarajan, Lele & Ferziger 2004). The unclosed subgrid terms are modelled with the dynamic Smagorinsky subgrid model generalized to a curvilinear coordinate system. Lengths, velocities and density are normalized by the leading-edge semi-major axis a^* (defined below), the speed of sound in the free-stream c_∞ and the free-stream density ρ_∞ respectively. Unless stated otherwise, all quantities are non-dimensional. Other normalization, such as the local boundary layer thickness for length or the free-stream or friction velocity for velocities, are explicitly stated when used.

The geometry consists of a flat plate fitted with a *super-ellipse* leading edge defined by

$$\frac{x^{*6}}{a^{*6}} + \frac{y^{*2}}{b^{*2}} = 1 \tag{2.16}$$

where the superscript * denotes dimensional quantities; a^* and b^* are the semi-major and semi-minor axes of the super-ellipse respectively. The aspect ratio of the leading edge is $AR = a^*/b^*$. With a^* as the reference length, the non-dimensional major and minor axes are $a = 1$ and $b = 1/AR$. The choice of exponents ensures that the leading edge does not have any sharp corners, while maintaining a very high level of continuity (up to the fifth derivative) at the junction of the flat plate and the leading edge. In this study, two leading edges of aspect ratio 10 and 6 are used. These are denoted by AR10 LE and AR6 LE respectively, and are characterized in table 1. The change in aspect ratio corresponds to a change of leading-edge diameter by a factor of 2.78.

https://doi.org/10.1017/S0022112006001893 Published online by Cambridge University Press

Leading edge	Major axis (a)	Minor axis (b)	Aspect ratio	LE diameter
AR 10 LE	2	0.2	10	0.06
AR 6 LE	2	1/3	6	0.166

TABLE 1. Characteristics of leading edges. All lengths are normalized by the semi-major axis of the leading-edge super-ellipse (see figure 1*b*).

A schematic of the domain used and the coordinate system is shown in figure 1(*b*). The Cartesian coordinate system used to describe the results has its origin at the forward stagnation point, with the x- and y-axes along and normal to the line of symmetry respectively. All lengths are normalized by the semi-major axis a of the leading-edge super-ellipse. The junction of the leading edge and the flat plate is therefore located at $x = 1$ and the surface of the plate is $y = 1/AR$ where AR is the aspect ratio of the leading-edge super-ellipse. Flow is from left to right, entering through the inflow boundary in figure 1(*b*), and carries with it grid turbulence of specified characteristics.

The governing equations are discretized on a structured C-mesh wrapped around the body, as shown in figure 1(*b*). For each case the two-dimensional grid generated consists of 720×97 points, of which 96 streamwise grid points are below the line of symmetry. As the geometry used herein is symmetric, simulation on one side of the body is sufficient. The domain in the lower half is therefore truncated to reduce computational cost. The two-dimensional grid is split into zones I and II with 53 and 44 points respectively in the wall-normal direction, and 80 and 40 points in the spanwise direction which has a dimension of 0.24, chosen to ensure sufficient de-correlation in the spanwise direction. The adequacy of the spanwise dimension is demonstrated through the spanwise two-point correlation of streamwise velocity u in figure 1(*c*). For a separation half the box size, the correlation drops to below 0.1 over the entire length of the plate indicating de-correlation of the spanwise structures for the given size. The total number of grid points in each case is 4.3 million. In cases A and B (introduced in later), the streamwise extent of the domain used was shorter, with only 640 grid points.

Simulations are initialized with a two-dimensional laminar flow solution over the flat plate with the leading edge. All simulations are conducted at a free-stream Mach number of 0.5 and a Reynolds number of $Re = U_\infty a/\nu = 50\,000$. The plates are at zero angle of attack and nominally in a zero pressure gradient flow. The laminar flow is obtained by first solving the compressible potential flow over the body, and then using the result to initialize a two-dimensional Navier–Stokes simulation. The code developed in Xiong (2004), following the work of Collis (1997) is used to obtain the steady laminar flow solution.

The laminar flow solution so obtained is used to initialize a three-dimensional turbulent flow simulation in which free-stream turbulence, obtained from simulations of homogeneous isotropic turbulence, is imposed at the inflow boundary. The isotropic turbulence simulations are carried out in boxes of size $4.8 \times 1.152 \times 0.24$ in the x-, y-, and z-directions respectively, and use $400 \times 96 \times 32$ grid points. These simulations are initialized with the von-Kármán spectrum

$$E(k) = \frac{u_{rms}^2}{C} L \frac{(kL)^4}{(1+(kL)^2)^p} \exp(-\alpha_k (kL)^2) \tag{2.17}$$

https://doi.org/10.1017/S0022112006001893 Published online by Cambridge University Press

	Case A	Case B	Case C	Case D	Case E
Leading edge	AR10 LE	AR10 LE	AR10 LE	AR6 LE	AR6 LE
Turbulence intensity Tu	3.5	4.5	4.5	4.5	3.5
Integral scale $\mathscr{L}$	0.03	0.03	0.045	0.045	0.03
$Re_{\mathscr{L}} = \mathscr{L}\sqrt{3}u_{rms}/\nu$	90	117	175	175	90

TABLE 2. Summary of simulations conducted.

where an exponential damping has been added at high wavenumbers to avoid instabilities in the transient. The exponent $p = 17/6$, and the normalization constant is

$$C = \frac{\sqrt{\pi}\Gamma(1/3)}{4\Gamma(17/6)}. \tag{2.18}$$

The high-wavenumber damping changes the characteristics of the initial field from those of the von Kármán spectrum. The desired characteristics are obtained by trial and error. The field is time advanced till the required length scale and intensity are reached. For each bypass transition simulation, many such realizations of isotropic turbulence are obtained, and the resulting boxes are joined using the procedure of Xiong, Nagarajan & Lele (2004) to provide the long time record required at the inflow plane. The incoming turbulence field is imposed in the form of a boundary condition along the inflow boundary (see figure 1*b*) using the one-dimensional unsteady form of the linearized characteristic-based boundary condition of Giles (1990). The turbulence field along the inflow boundary is multiplied by a damping function that takes the value 1 along the inflow boundary upstream of the leading edge and reduces to 0 on the same boundary above the plate. The outflow boundary, which intersects the boundary layer developing on the flat plate is specified using the parabolized form of the Navier–Stokes equations (Collis 1997) with an imposed pressure gradient that is obtained from the compressible potential flow solution.

In addition to the leading-edge aspect ratio, the characteristics of the imposed free-stream turbulence are also varied for a total of five simulations, summarized in table 2.

Cases A to C use AR10 LE whereas cases D and E use AR6 LE. Between cases A and B, the only parameter that differs is the intensity of the free-stream turbulence. Comparing these two cases therefore brings out the effect of turbulence intensity on transition. From case B to C, the integral scale of free-stream turbulence is changed to study the effect of length scale on transition. The effect of leading-edge bluntness is may be assessed by comparing cases C and D and also cases E and A.

2.3. *Resolution check*

Simulations of transitional and turbulent boundary layers have evolved to an extent that the resolution requirements are now known *a priori*. Based on their numerical experiments and simulations conducted earlier, Jacobs & Durbin (2001) show that a resolution of about $\Delta x^+ \sim 15$ and $\Delta z^+ \sim 8$ is required for accurate prediction of skin friction in a transitional boundary layer. Lower resolution usually causes the skin friction to overshoot the turbulent value post-transition. On the other hand, the first grid point in the wall-normal direction usually needs to be below $\Delta y^+ = 0.4$.

The maximum value of the mean friction velocity u_τ in each case is used to quantify the resolution of the simulations. The resolution in terms of wall units for the five

https://doi.org/10.1017/S0022112006001893 Published online by Cambridge University Press

	Δx^+	Δy_w^+	Δz^+	N_{grid}
Case A	41	0.50	8	3.8
Case B	45	0.54	9	3.8
Case C	45	0.54	9	4.3
Case D	49	0.78	10	4.3
Case E	49	0.78	10	4.3
Jacobs & Durbin (2001)	12	< 0.4	6	71

TABLE 3. Resolution in wall units. N_{grid} is the number of grid points in millions.

simulations is shown in table 3. Also shown are the corresponding values used by Jacobs & Durbin (2001). It should be kept in mind that the high-order compact schemes used here have much better resolving power (Nagarajan, Lele & Ferziger 2003) than the second-order staggered method used by Jacobs & Durbin (2001). As a result, half the number of grid points in each direction provide similar accuracy as Jacobs & Durbin (2001). A grid resolution of $\Delta y^+ < 0.4$ at the wall is fine enough to resolve the viscous sublayer. The spanwise resolution in the boundary layer, of the order of $\Delta z^+ \sim 8 - 10$, is comparable to that of Jacobs & Durbin (2001). This is also fine enough to resolve most spanwise scales. Note also that the wall-normal and spanwise grid become much coarser away from the wall. The overall resolution of these simulations is comparable to that of Jacobs & Durbin (2001) inside the boundary layer, except in the streamwise direction in which the grid size is larger in the present simulations. While the flow in the boundary layer is fairly well resolved, in zone II the smaller number of spanwise grid points along with stretching in the wall-normal direction makes our simulations LES in this region, especially in the region upstream of the flat plate.

3. Characterization of mean flow field and turbulence

3.1. *Laminar flow over the blunt-nosed flat plate*

The grid size in the free stream (above the flat plate) needs to be small enough to resolve the free-stream turbulence. As a result, the vertical size of the domain is limited by computer constraints; a large domain will need a large number of grid points. This size limitation causes the mean velocity, and therefore the Reynolds number, on the flat plate to be different from the imposed free-stream condition. The streamwise velocity along the inflow boundary, from the stagnation to the outflow plane, is shown in figure 2(*a*) for the two bodies. The velocity does not recover the free-stream value of 0.5 in either case. The corresponding pressure coefficient $C_p = 2(p - p_{ref})/\rho_{ref} U_{ref}^2$, where the reference quantities have been chosen to be the mean value above the flat plate, is shown in figure 2(*b*). Even though the velocity and pressure over the flat plate are not equal to the respective free-stream values, both remain fairly uniform over the entire length of the flat plate, a characteristic of zero-pressure-gradient boundary layers. This is also shown in figure 2(*c*), which plots the pressure gradient parameter λ defined as

$$\lambda = \frac{\theta^2}{\nu} \frac{\mathrm{d}U}{\mathrm{d}x} \tag{3.1}$$

that is used to characterize boundary layers with pressure gradients. The parameter shows a favourable and an adverse pressure gradient region near the leading edge.

https://doi.org/10.1017/S0022112006001893 Published online by Cambridge University Press

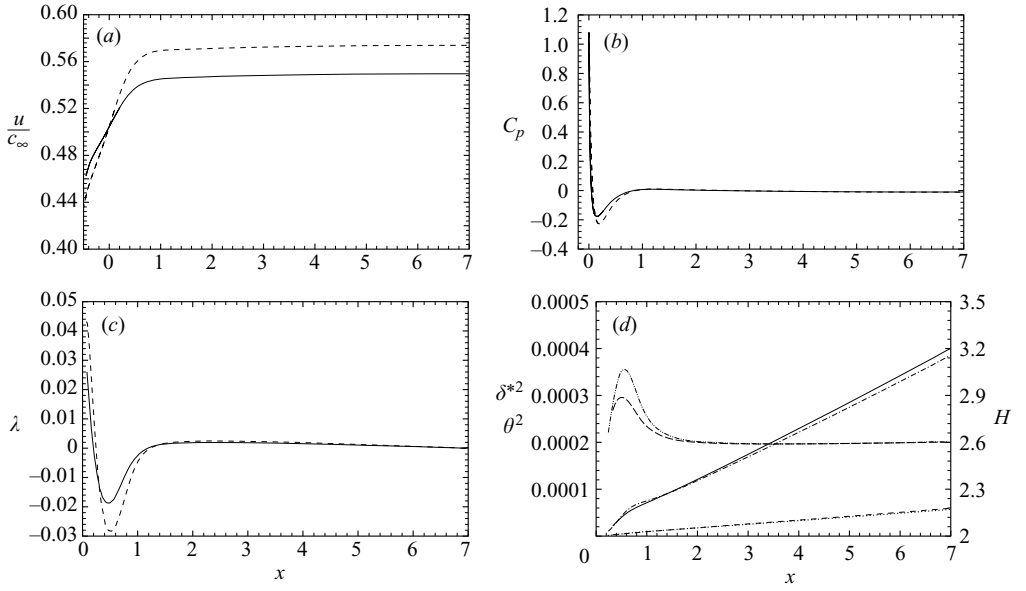


FIGURE 2. Laminar flow characteristics of the two leading edges. (*a*) Streamwise velocity along the inflow boundary. (*b*) Pressure coefficient C_p along the surface of the plate as a function of x. (*c*) Pressure gradient parameter $\lambda = (\theta^2/\nu)(\mathrm{d}U/\mathrm{d}x)$ as a function of x. (*d*) Streamwise development of square of displacement thickness (δ^*), square of momentum thickness (θ), and shape factor ($H = \delta^*/\theta$). In (*a–c*), ——, AR10 LE; ----, AR6 LE. In (*d*) ——, δ^{*2} AR10 LE; —·—, δ^{*2} AR6 LE; ----, θ^2 AR10 LE; ····, θ^2 AR6LE; ——, H AR10 LE; —··—, H AR6 LE.

Furthermore, λ is very close to zero over the entire length of the flat plate, indicating that the boundary layer is indeed a zero-pressure-gradient one.

The primary effect of incomplete recovery of the free stream is a change in the effective Reynolds number, which may be estimated from the development of the boundary layer displacement thickness over the flat plate. In figure 2(*d*), the square of the displacement thicknesses δ^* over the two flat plates is plotted as a function of streamwise location x. The Blasius boundary layer relation between δ^* and x (White 1991) is used to estimate the Reynolds number based on reference length a as

$$Re_a = \frac{Ua}{\nu} = \frac{1.7208^2}{\mathrm{d}\delta^{*2}/\mathrm{d}x}.$$

Alternatively, the effective Reynolds number may be evaluated from the development of the square of the momentum thickness θ^2 with streamwise distance x, also shown in figure 2(*d*). The two values obtained independently from displacement and momentum thickness are within 1 % of each other. Their average is taken to be the Reynolds number, which is 54 000 and 57 000 for AR10 LE and AR6 LE respectively. Using Blasius boundary layer theory, a virtual origin can also be located. For the boundary layer developing over the flat plate, this corresponds to the location at which the boundary layer would have zero thickness. For AR10 LE and AR6 LE, the virtual origins are 0.19 and 0.28 non-dimensional units upstream of the actual stagnation point. In the results presented in the following sections, the distance from the leading edge x and the Reynolds number $Re_x = Ux/\nu$ are used interchangeably. The two

https://doi.org/10.1017/S0022112006001893 Published online by Cambridge University Press

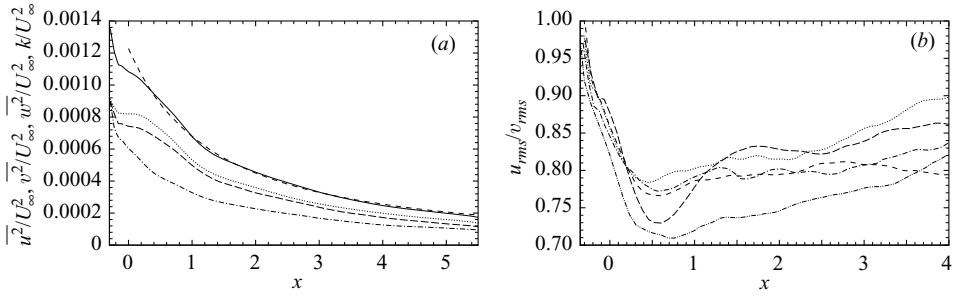


FIGURE 3. (*a*) Streamwise variation of decay of various components of kinetic energy in case A. ——, k; - - - -, curve fit using equation (3.4); —·—, $\overline{u^2}$; · · · ·, $\overline{v^2}$; ——, $\overline{w^2}$. (*b*) Streamwise variation of anisotropy u_{rms}/v_{rms} of the free-stream turbulence above the plate. - - - -, case A; —·—, case B; · · · ·, case C; ——, case D; —··—, case E.

variables are related through the quantities Re_a and the virtual origin x_0. For the two leading edges, the expressions that relate x and Re_x are

$$Re_x = (x + 0.19) \times 54000 \qquad \text{for AR10 LE,} \tag{3.2}$$

$$Re_x = (x + 0.28) \times 57000 \qquad \text{for AR6 LE.} \tag{3.3}$$

3.2. *Downstream development of free-stream turbulence*

Precomputed homogeneous isotropic turbulence is imposed at the inflow boundary upstream of the leading edge, i.e. on the vertical portion of the inflow boundary. The imposed field is damped to zero as the inflow boundary turns and becomes horizontal. In the vertical region, the mean velocity is fairly uniform (see figure 2(*a*) in the region $x < -0.1$) and therefore its distortion effect on turbulence is not expected to be significant. It should be noted that even though there will be some distortion of turbulence by small gradients upstream of the inlet, the bulk of the distortion is due to the mean velocity gradients inside the domain. The resulting turbulent field that interacts with the boundary layer developing on the flat plate is therefore non-isotropic. Figure 3(*a*) shows the development of the RMS of velocity fluctuations in the free stream ($2.5\delta_{99}$ away from wall, where δ_{99} is the 99 % thickness of the laminar boundary layer) from the simulation case A. As a result of distortion of turbulence by the leading edge, usually in the form of stretching and tilting of vortices initially oriented in the y-direction, the level of streamwise velocity fluctuation is lowered while the spanwise and wall-normal components are increased, a trend evident in all simulations. This process continues in the outer region as turbulence convects downstream, till it reaches a point where the mean flow becomes more uniform and the associated mean strain rate reduces. For all cases, this occurs around $x \sim 0.5$, and the turbulence starts to recover downstream of this location. This is more evident from the location of minima in figure 3(*b*) which shows the anisotropy u/v versus downstream distance. As the amplification of v exceeds that of w, the measure u/v is consistently lower than u/w. For the case of the blunter leading edge, the turbulence becomes more anisotropic with $u/v \sim 0.72$ compared to ~ 0.77 for the sharper leading edge.

It is common practice to express the decay of kinetic energy k in grid turbulence in the form of a power law

$$\frac{k}{U_\infty^2} = A\,(x - x_0)^{-n} \tag{3.4}$$

https://doi.org/10.1017/S0022112006001893 Published online by Cambridge University Press

Case	A	B	C	D	E
n	1.34	1.43	1.53	1.54	1.32

TABLE 4. Decay exponent for free-stream turbulence.

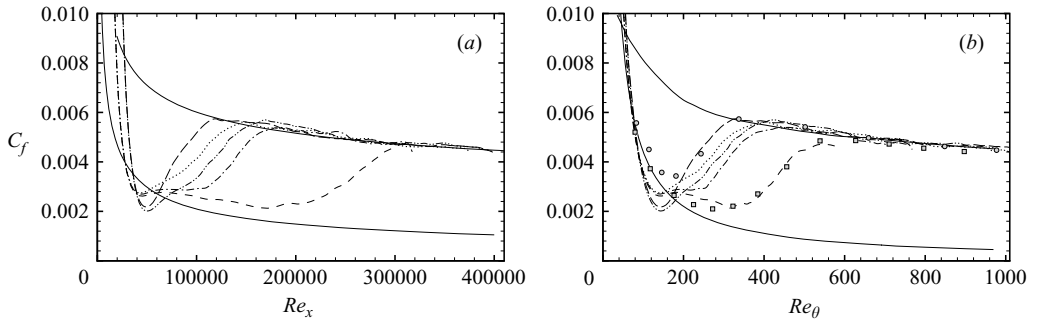


FIGURE 4. Skin-friction coefficient C_f as a function of Reynolds number (*a*) Re_x and (*b*) Re_θ. ----, Case A; —·—, Case B; ····, Case C; ——, Case D; —··—, Case E; ——, Blasius boundary layer and turbulent boundary layer correlation; □, Case T3A; ○, Case T3B of Roach & Brierley (1992).

where the exponent n represents the rate of decay, x_0 is the virtual origin and A is a normalization constant. In the literature, values of n over a very wide range have been reported but $n = 1.3$ may be considered representative (Mohamed & LaRue 1990). The decay exponent n for turbulence above the flat plate is evaluated using a least-squares fit for k using equation (3.4). In evaluating the exponent, the anisotropic initial portion of the field (over the leading edge) is ignored. The resulting values of the exponent are tabulated in table 4. Due to anisotropy, the agreement between the turbulence and the curve fit is not as good as one would get for isotropic turbulence. Case E which corresponds to the most energetic turbulence undergoing the maximum amount of distortion shows the largest deviation from the curve fit at upstream locations. However, for this as well as all other cases, the decay exponent remains fairly close to the accepted value, and within the range reported in the literature. They are, in general, higher for lower Reynolds numbers. Cases A and E and C and D use the same turbulence field with different leading edges. The decay exponents are, however, quite close.

3.3. *Mean flow and statistics in the boundary layer*

In figures 4(*a*) and 4(*b*), the coefficient of skin friction is shown as functions of Re_x and Re_θ, respectively. For $Re_x < 50\,000$, the skin friction is lower than the Blasius value even though the boundary layer is laminar. This is due to the fact that this Reynolds number range corresponds to the leading-edge region with a slight adverse pressure gradient (see figure 2*b*) which causes the boundary layer to thicken, thus lowering the skin friction. Downstream of the leading edge, in case A, the skin-friction coefficient shows signs of recovering the laminar value, as evident from the change in slope around $Re_x \sim 60\,000$ and $Re_\theta \sim 160$ in figures 4(*a*) and 4(*b*) respectively. However, due to forcing by the imposed free-stream turbulence, the boundary layer is no longer laminar. In this *buffeted boundary layer* driven by external turbulence,

https://doi.org/10.1017/S0022112006001893 Published online by Cambridge University Press

Case	U_∞ (m/s)	Tu	$\mathscr{L}$ (mm)
T3A	5	3	9
T3B	9.2	6	12.5

TABLE 5. ERCOFTAC cases T3A and T3B from Roach & Brierley (1992). The integral length scales are the estimates of Johnson & Ercan (1999).

the skin-friction coefficient is higher than the laminar value, and continues to be so until the onset of transition around $Re_\theta \sim 300$. On the other hand, cases B through E never recover fully from the adverse pressure gradient effect. Transition onset occurs around $Re_\theta \sim 200$, immediately downstream of the leading edge. Of these, only case B shows some sign of recovery from the pressure gradient effect.

Also shown in figure 4(*a*) are the laminar Blasius value and the turbulent correlation (White 1991)

$$C_f = \frac{0.455}{\ln^2(0.06Re_x)}. \tag{3.5}$$

Since the correlation is based on Re_x, curves corresponding to each simulation on the C_f vs. Re_θ plot are different in the turbulent zone. As the turbulent correlation shown in figure 4(*b*) corresponds to case B, the other cases, especially case A, show some scatter from this curve. On the other hand, all five simulations agree with the turbulent correlation on the C_f versus Re_x plot shown in figure 4(*a*). Note that the skin-friction overshoot above the turbulent correlation is very small. Jacobs & Durbin (2001) observed this to be a function of the streamwise resolution of the boundary layer. The small overshoot indicates that the resolution in these simulations is adequate.

The simulation conditions were not chosen to match any particular experiment. However, as seen from table 5, the conditions for simulation case A results are compared to the ERCOFTAC transition case T3A (Roach & Brierley 1992). The experiment is conducted at a free-stream turbulence level of 3 % and the characteristic length scale of free-stream turbulence is $4\delta_{99}$ where δ_{99} is the laminar boundary layer 99 % thickness at a Reynolds number of $Re_x = 50\,000$. The turbulence intensity at the inflow plane in case A is comparable to T3A whereas the length scale is only $1.3\delta_{99}$. Therefore, at a comparable location, the turbulence level in the simulation is lower while there is a factor of three difference in length scales between the experiments and simulation. Furthermore, the leading edge in the simulation is much blunter than the one used in the experiments. Therefore, the comparison between case A and experiments should be taken as a qualitative confirmation of the transition process rather than a strict quantitative comparison. The variation of skin-friction coefficient C_f with Re_θ is in good agreement with experimental data, as shown in figure 4(*b*). In the simulations, as in the experiments, the skin-friction coefficient indicates that transition onset is around $Re_\theta \sim 300$ and is complete by $Re_\theta \sim 600$. However, the simulated skin-friction coefficient in the pre-transitional *buffeted boundary layer* is slightly higher than in the experiment (which remains fairly close to the Blasius value). This trend, also seen in the results of Jacobs & Durbin (2001), may be attributed to the smaller turbulence length scale in the simulations. Due to the smaller length scale, the free-stream turbulence in the simulations has more energy in structures with characteristic spanwise length scales comparable to the boundary layer thickness.

https://doi.org/10.1017/S0022112006001893 Published online by Cambridge University Press

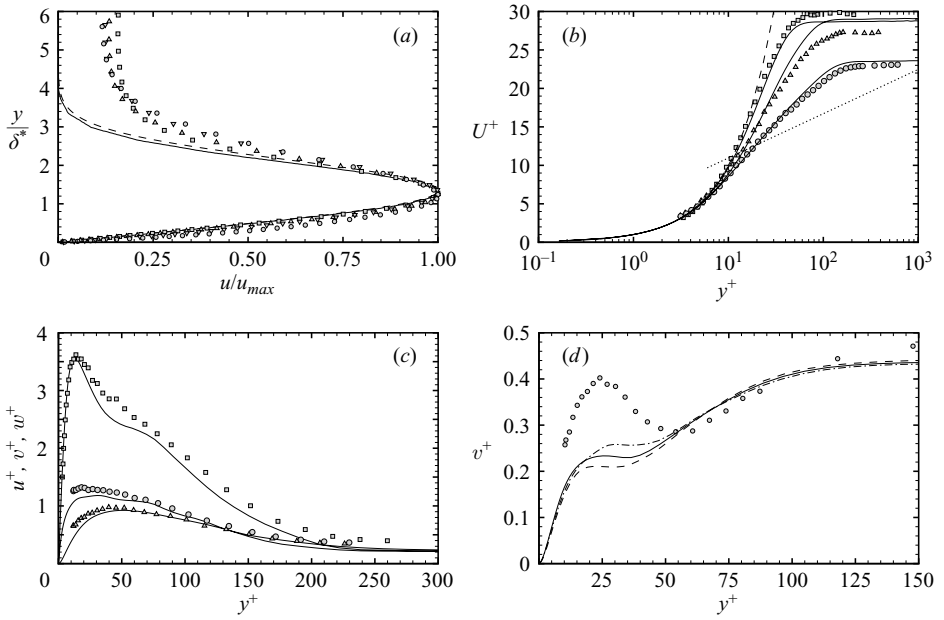


FIGURE 5. (*a*) Normalized profiles of RMS velocity fluctuation compared to optimal disturbances. ——, Optimal disturbance; ----, Crow (1966); □, $Re_x = 6 \times 10^4$; △, $Re_x = 8 \times 10^4$; ▽, 10×10^4; ○, 12×10^4. (*b*) Evolution of mean velocity profiles in case A compared to the experiments of Roach & Brierley (1992). Symbols are experimental data points □, $Re_\theta = 225$; △, $Re_\theta = 385$; ○, $Re_\theta = 456$; ----, $U^+ = y^+$; ····, Log law. (*c*) Profiles of RMS velocity fluctuation at $Re_\theta = 456$ compared to the experiments of Roach & Brierley (1992). Symbols are experimental data points □, u^+; △, v^+; ○, w^+. (*d*) Profiles of RMS wall-normal velocity fluctuation. ----, $Re_\theta = 220$; ——, $Re_\theta = 225$; —·—, $Re_\theta = 230$; ○, Roach & Brierley (1992) at $Re_\theta = 225$.

These structures affect the pre-transitional region as they penetrate into the boundary layer far more effectively (Andersson *et al.* 1999; Luchini 2000; Leib *et al.* 1999). Mean velocity profiles based on wall units are compared at three values of Re_θ in figure 5(*b*). Profiles are in agreement over a wide range of Reynolds numbers over which the boundary layer develops from a laminar to a turbulent one. However, the simulation does not include a fully turbulent boundary layer and a distinct logarithmic region is therefore absent. Profiles of RMS velocity fluctuation at $Re_\theta = 456$ are shown in figure 5(*c*). The computation slightly under-predicts levels in the RMS velocity but is in very good qualitative agreement with experimental observations. Jacobs & Durbin (2001) observe that the v^+ profile from the experiment shows a peak near $y^+ \sim 25$ for $Re_\theta = 225$, which was absent in their simulation. The profiles at and near $Re_\theta = 225$ from the present computation, shown in figure 5(*d*), have a minor peak that is much smaller than in the experiment.

A comparison between normalized RMS streamwise velocity profiles and linear optimal disturbances (Andersson *et al.* 1999; Luchini 2000) is shown in figure 5(*a*). Also shown is the result from the analysis of Crow (1966) (this expression was first used by Taylor 1939). The RMS velocity profiles are in the pre-transitional region ($Re_x = 60\,000$ to $= 120\,000$) and normalized by the local maximum in the RMS profile. The disturbances in the pre-transitional region are in good agreement with the optimal streak as well as the perturbed boundary layer analysis.

https://doi.org/10.1017/S0022112006001893 Published online by Cambridge University Press

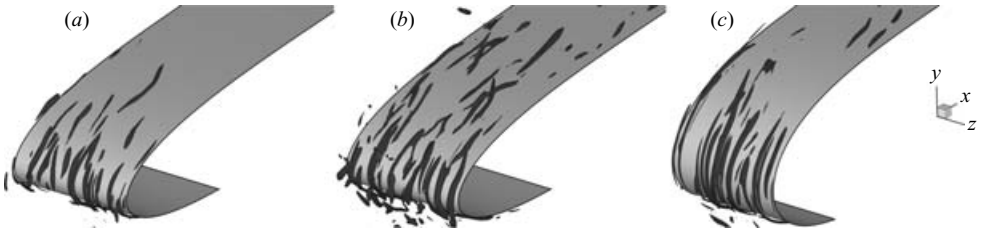


FIGURE 6. Vortices identified by an iso-surface of λ_2. (*a–c*) Cases A, B, and E.

The skin-friction plots 4(*a*) and 4(*b*) also reproduce the trends observed in experiments. With an increase in the turbulence intensity from case A to case B, onset of transition moves upstream as has been observed in many experiments (Roach & Brierley 1992; Westin *et al.* 1994; Matsubara & Alfredsson 2001). This effect is well known and is included in correlations such as those of Abu-Ghannam & Shaw (1980). Furthermore, as observed in the experiments of Jonas, Mazur & Uruba (2000), the increase in the integral length scale from case B to C, while holding the intensity fixed, also moves the transition location upstream.

4. The mechanisms of transition

The results from the previous section show a clear effect of the leading edge on the onset of transition. Under given free-stream conditions, a blunter leading edge exhibits earlier onset and completion of transition. Furthermore, as will be shown in this section, increasing the intensity of the free-stream turbulence also moves transition upstream through a similar process, though other well-known effects of intensity and length scale on bypass transition are also at play. To understand these effects, cases A, B and E are studied further. Cases C and D also show similar trends, but are not included as the differences between them are not large enough to throw enough light on leading-edge effects.

4.1. *Distortion of turbulence by the leading edge*

Goldstein & Wundrow (1998) argue that the distortion of turbulence by the mean flow around the leading edge causes wake-like disturbances in the free-stream turbulence to be transformed into streamwise aligned vortices. These vortices then penetrate into the boundary layer to form Klebanoff modes. In subsequent work, Wundrow & Goldstein (2001) analyse the effect of streamwise vorticity in the free stream on a boundary layer and show that it can lead to low- and high-speed streaks. Clearly, the leading edge does cause amplification of streamwise vortices, as can be seen from the anisotropy in figure 3(*b*). To see the extent of this amplification, vortex cores are identified using the λ_2 method of Jeong & Hussain (1995), wherein a vortex is defined to be a region where two eigenvalues of the tensor $S^2+\Omega^2$ are negative, i.e. the regions inside iso-surfaces of $\lambda_2=0$, where the λ are the eigenvalues arranged in increasing order. Generally, $\lambda_2=0$ has been found to be an inadequate criterion. Vortices are better identified by $\lambda_2=C$, where C is a negative number. In figure 6, iso-surfaces of $\lambda_2=-15$ are shown in the leading-edge region. The vortices in case A are weaker and less numerous than in case B. This is to be expected as the FST in case A is less intense and therefore the free-stream vorticity level is lower. Furthermore, leading edge vortices in case A are also less intense than case E because the total distortion

https://doi.org/10.1017/S0022112006001893 Published online by Cambridge University Press

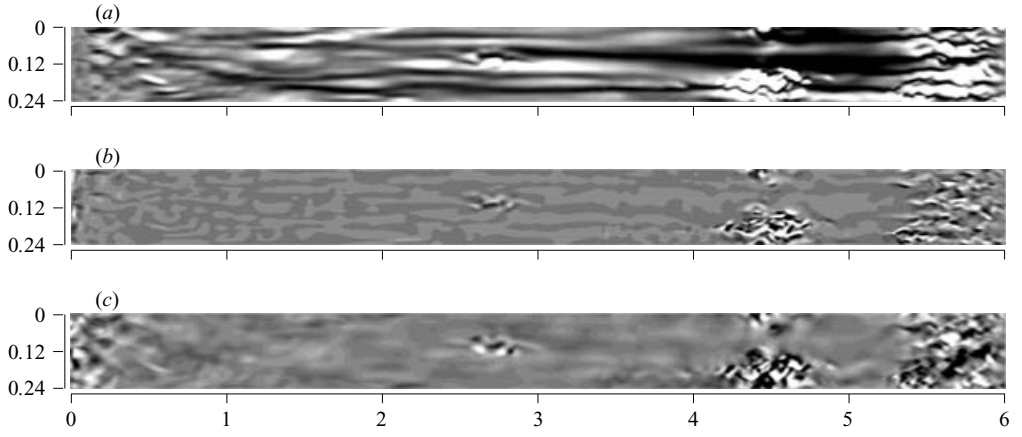


FIGURE 7. Plan-view (x, z-plane) of the flat plate from case A showing streaks, a turbulent spot and an incipient spot. z-coordinate is magnified by a factor of 2. (a) Snapshot of u-velocity ($-0.1 < u/U_\infty < 0.15$). (b) Snapshot of v-velocity ($-0.04 < v/U_\infty < 0.04$). ($c$) Snapshot of w-velocity ($-0.08 < w/U_\infty < 0.08$).

in case A is lower. The vortex visualization plots also indicate that the vortices in cases B and E extend further downstream from the leading edge than in case A.

4.2. *Bypass transition – case A*

Pre-transitional boundary layers forced by free-stream turbulence have been observed (Klebanoff *et al.* 1962; Kendall 1991; Westin *et al.* 1994; Matsubara & Alfredsson 2001) to contain streamwise elongated streaks with a spanwise scale comparable to the boundary layer thickness. It has also been shown that streamwise aligned counter-rotating vortices can cause alternating high- and low-speed streaks in the boundary layer through transient growth (Andersson *et al.* 1999; Luchini 2000). It has also been proposed in the literature that bypass transition occurs due to a secondary instability of the streaks (Andersson *et al.* 2001; Brandt & Henningson 2002) wherein sinuous and varicose streak modes come into play. While the backward jet mechanism of Jacobs & Durbin (2001) seems to be the same as the streak sinuous mode, they do not report the varicose mode.

In this section, it is demonstrated that such a path (streak instability/backward jet) to transition exists when the leading edge is sharp and the turbulence relatively weak (case A). Boundary layer streaks along with a turbulent spot and a fully turbulent zone are evident in figure 7 which shows snapshots of velocity fluctuations from case A. It should be kept in mind that, for improved clarity, the z-axis has been magnified by a factor of 2. The streaks and spots are therefore much narrower than they appear. The streamwise component of the velocity shows distinct low- and high-speed regions upstream of the spot. In fact, these streaks persist even downstream of the turbulent spot. This suggests that the spots are formed by local instabilities and not a global streak instability. The structures inside the turbulent spot are more evident in the snapshot of wall-normal and spanwise velocity fluctuations. A zoomed-in view of the spot is shown in figure 7. Clearly, the length scales inside the spot are much shorter and more diverse than in the buffeted boundary layer. This broadband nature is characteristic of turbulent flow. As in the simulations of Jacobs & Durbin (2001) and Brandt *et al.* (2004), spots are formed by instabilities growing on low-speed streaks.

https://doi.org/10.1017/S0022112006001893 Published online by Cambridge University Press

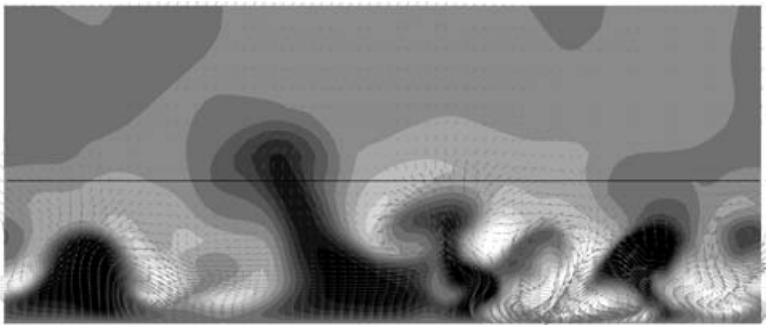


FIGURE 8. Cross-section (z, y-plane) of the turbulent spot from figure 7. Contours of streamwise velocity and velocity vectors in the plane. y-coordinate is magnified by a factor of 2. The line denotes the edge of the boundary layer.

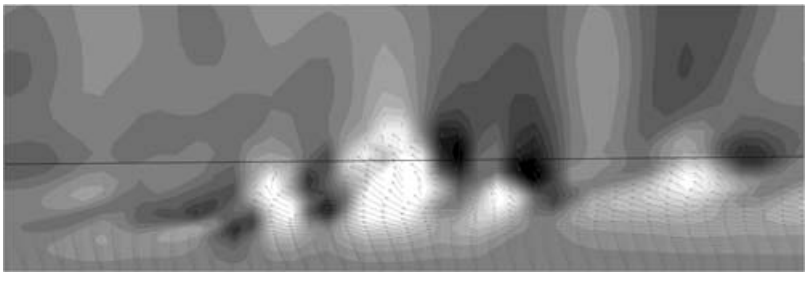


FIGURE 9. Visualization, in the (x, y)-plane, of the early stages of the spot from figure 7. Wall-normal velocity contours with velocity vectors in the plane. y-coordinate is magnified by a factor of 2. The line denotes the edge of the boundary layer.

A visualization of a spot cross-section in figure 8 shows the large velocity vectors in the (z, y)-plane to be concentrated in regions of low streamwise velocity, indicated by dark colours. The instigation of instability of a low-speed streak is seen in figure 9 that shows an (x, y)-plane passing through an incipient spot. The velocity vectors in the plane show the low-speed streak interacting with a free-stream eddy depicted by contours of wall-normal velocity. Plan-views of contours of streamwise, wall-normal and spanwise velocities in figures 10(a), 10(b) and 10(c) show the early stages of a spot. The instability is triggered in the outer half of the boundary layer and the fluid close to the wall remains unaffected in the early stages of spot formation. This can be seen from figure 10(d) wherein the spanwise velocity disturbance is seen to be large at $y/\delta_{99,loc} \sim 0.5$ ($\delta_{99,loc}$ being the local laminar boundary layer 99 % thickness) and decays rapidly towards the wall. At $y/\delta_{99,loc} \sim 0.25$, the disturbance is small whereas it is fairly prominent at $y/\delta_{99,loc} \sim 0.75$. The lower part of the boundary layer (and hence the skin friction) is affected only after the instability grows and further breakdown leads to spot formation. Therefore, it may be concluded that when leading-edge effects are unimportant, as in case A, formation of turbulent spots occurs through the instability brought about by interaction of a low-speed streak with a free-stream eddy, as observed by Jacobs & Durbin (2001) and Brandt *et al.* (2004). However, when leading-edge effects are dominant, other mechanisms take over, as demonstrated in the remainder of this paper.

https://doi.org/10.1017/S0022112006001893 Published online by Cambridge University Press

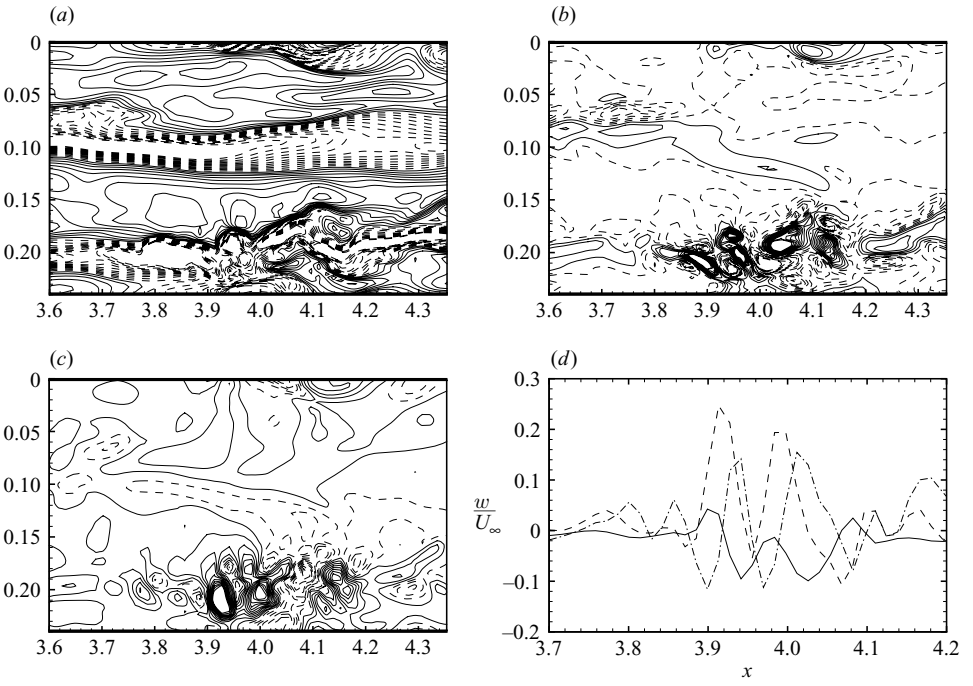


FIGURE 10. Structure of the low-speed streak sinuous mode/backward jet precursor to a turbulent spot from case A. Shown are plan views of (*a*) *u*-, (*b*) *v*- and (*c*) *w*-velocity contours on a plane at $y = \delta_{99,loc}/2$. (*d*) Spanwise velocity fluctuation versus streamwise coordinate. ——, $y/\delta_{99,loc} = 0.25$; - - - -, $y/\delta_{99,loc} = 0.5$; —·—, $y/\delta_{99,loc} = 0.75$.

4.3. *Transition with leading-edge effects – cases B to E*

In this section, the primary effect of the leading edge is introduced. In figure 11, a sequence of snapshots tracks the formation of turbulent spots in case B. The plan-view shows contours of spanwise velocity fluctuation at a distance of $y \sim \delta_{99}/4$ from the wall, where δ_{99} is the boundary layer thickness at the junction of the leading edge and the flat plate. Wavepacket-like precursors to spots are clearly visible in these snapshots. They appear to grow over the background disturbance inside the boundary layer, and eventually dominate the motion. They then continue to grow in size and increase in amplitude before breaking down into a patch of turbulence. Time sequence snapshots of spanwise velocity in a spot precursor are shown as a function of the streamwise coordinate in figure 12. The first snapshot in this time sequence shows a small-amplitude wavepacket-like disturbance. In the second and third snapshots, the amplitude of the disturbance increases as does the number of crests and troughs. In the fourth and fifth snapshots, the distinct wavepacket structure is lost as energy shifts to lower as well as higher wavenumbers. Subsequent snapshots show the appearance of many more length scales and the formation of a spot. From the transition process observed from these pictures the low-speed streak instability route can be discounted. This is illustrated by a magnified view of the *u*, *v* and *w* velocity fluctuations in a precursor to a spot from case B shown in figures 13(*a*), 13(*b*) and 13(*c*) respectively. The structure is wavepacket-like in the streamwise direction. This structure of the spot precursor is shown in figure 13(*d*) where the spanwise velocity is plotted versus the streamwise coordinate. There is a clear dominant wavelength corresponding to

https://doi.org/10.1017/S0022112006001893 Published online by Cambridge University Press

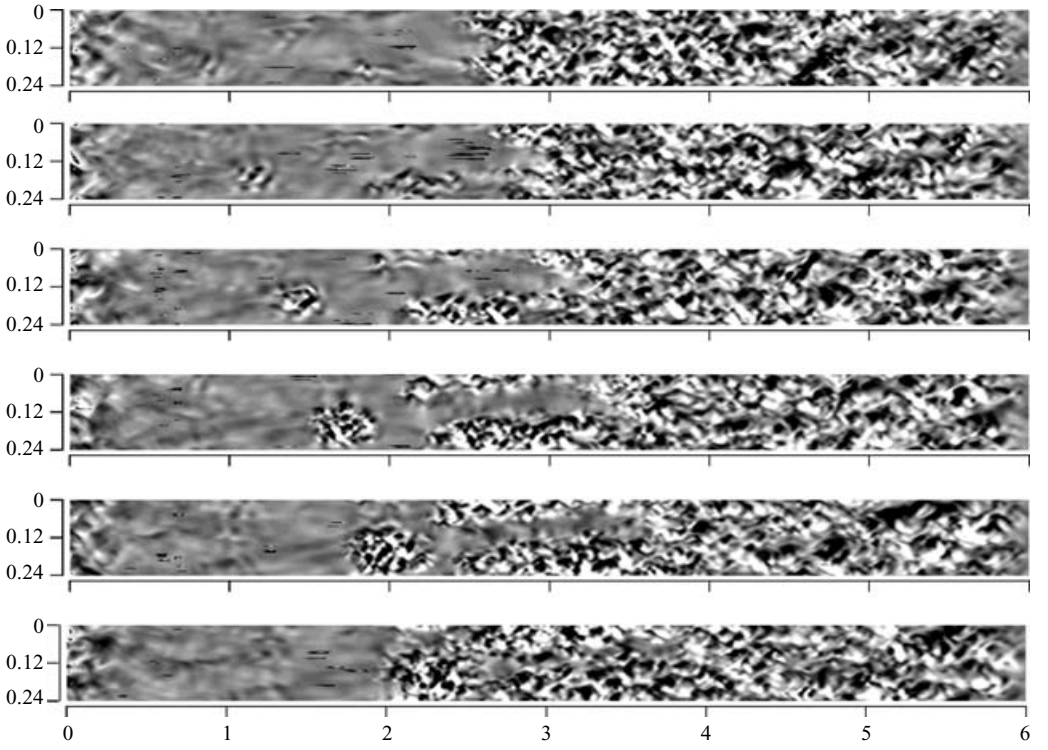


FIGURE 11. Plan-view (x, z-plane) of the flat plate from case B showing incipient spots, their growth and eventual merger with the fully turbulent boundary layer. Snapshots of w-contours ($-0.08 < w/U_\infty < 0.08$) separated by $\Delta t = 0.75$. z-coordinate is magnified by a factor of 2. The implied spot trailing- and leading-edge velocities are $0.55U_\infty$ and $0.73U_\infty$ respectively.

the oscillations inside the wavepacket, and an amplitude envelope that decays rapidly towards the edges of the structure. In addition, the streamwise velocity contours show that the precursor is overlaid on streaks in the boundary layer, but is not located on a low-speed streak, an essential component of the sinuous instability route to transition observed by Brandt *et al.* (2004) and Jacobs & Durbin (2001) as well as in case A. As a demonstration of the universality of spot precursors in cases B to E, the x-variation of spanwise velocity in a precursor from case E is shown in figure 14(*b*). All the spot precursors examined in cases B, C, D and E show such a wavepacket-like structure.

The turbulence level in case A is 3/4 that of case B, while all other parameters are the same. Due to such a small difference in the conditions, one might expect to occasionally see turbulent spots being formed by the same mechanism that operates in cases B to E. It has been observed that turbulent spots are indeed formed from wavepacket-like spot precursors in case A as well. For example, the incipient spot in the middle of the domain in figure 7 is preceded by steepening and breaking down of precursors inside the boundary layer. Therefore, in case A, both mechanisms of spot formation are present: (i) breakdown through interaction of low-speed streaks with free-stream disturbances, and (ii) through spot precursors. However, the second mechanism occurs infrequently and most turbulent spots are formed by the first.

https://doi.org/10.1017/S0022112006001893 Published online by Cambridge University Press

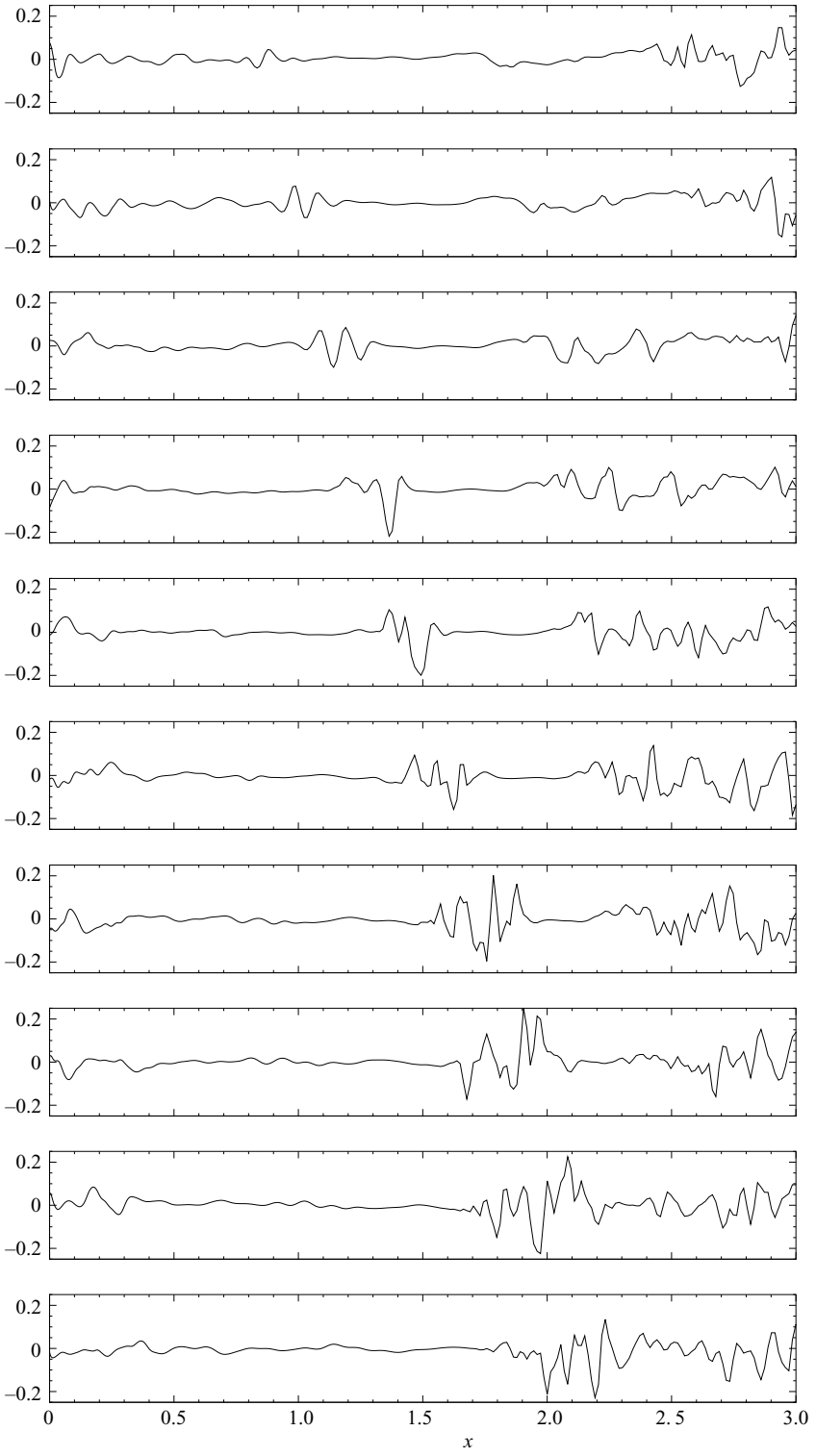


FIGURE 12. Snapshots of streamwise profile of spanwise velocity fluctuations from case B. Consecutive figures separated by $\Delta t = 0.375$.

https://doi.org/10.1017/S0022112006001893 Published online by Cambridge University Press

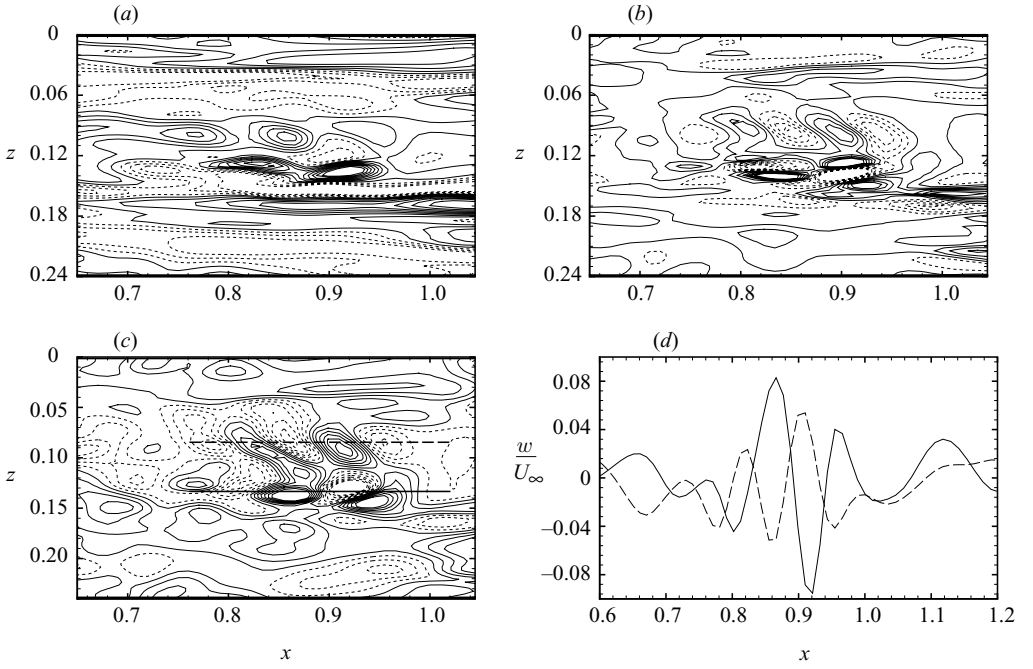


FIGURE 13. Structure of the precursor to a turbulent spot from case B. Shown are plan views of (*a*) *u*-, (*b*) *v*- and (*c*) *w*-velocity contours on a plane at $y = \delta_{99,loc}/4$. (*d*) Spanwise velocity fluctuation versus streamwise coordinate along lines —— and —— drawn in (*c*).

4.4. *Characterization of spot precursors*

A typical precursor to a turbulent spot is studied in detail to provide a complete picture of their characteristics. In figure 16(*a*), contours of spanwise velocity are shown in an (x, y)-plane passing though a wavepacket. Unlike the disturbances in figure 10 that are typical of bypass transition by low-speed streak instability, this is confined to the lower half of the boundary layer as also depicted in figure 16(*b*) where the spanwise velocity fluctuation is shown versus the streamwise coordinate at three wall-normal locations, $y/\delta_{99,loc} = 0.25, 0.5$ and 0.75, $\delta_{99,loc}$ being the local laminar boundary layer 99 % thickness. The amplitude of the oscillations is higher closer to the wall, and decreases rapidly away from the plate. Wall-normal profiles of disturbance velocities shown from case E in figure 16(*c*), while confirming that these wavepackets inhabit the lower half of the boundary layer, also highlight another difference between the formation of turbulent spots in this case and the sinuous streak instability. The spot precursor is localized in a region of large surplus velocity with respect to the mean, in marked contrast to the disturbances in figures 8 and 9 which usually occur in regions of relatively slow moving fluid. These two fundamental differences are highlighted in figures 15(*a*) and 15(*b*) that show contours of spanwise velocity fluctuations in an (x, y)-plane passing through the spot precursor, along with in -plane fluctuating velocity vectors. Figure 15(*a*) corresponds to the low-speed streak mechanism in the initial stages of the developed turbulent spot at $x \sim 4.5$ in figure 7. The slower moving fluid (left pointing vectors) and the initial stages of spot development in the outer half of the boundary layer are evident. On the other hand, 15(*b*) corresponds to the initial stages of the nascent spot at $x \sim 2.8$ in figure 7. This picture, typical of all spot precursors formed under leading-edge influence, shows the disturbance to be

https://doi.org/10.1017/S0022112006001893 Published online by Cambridge University Press

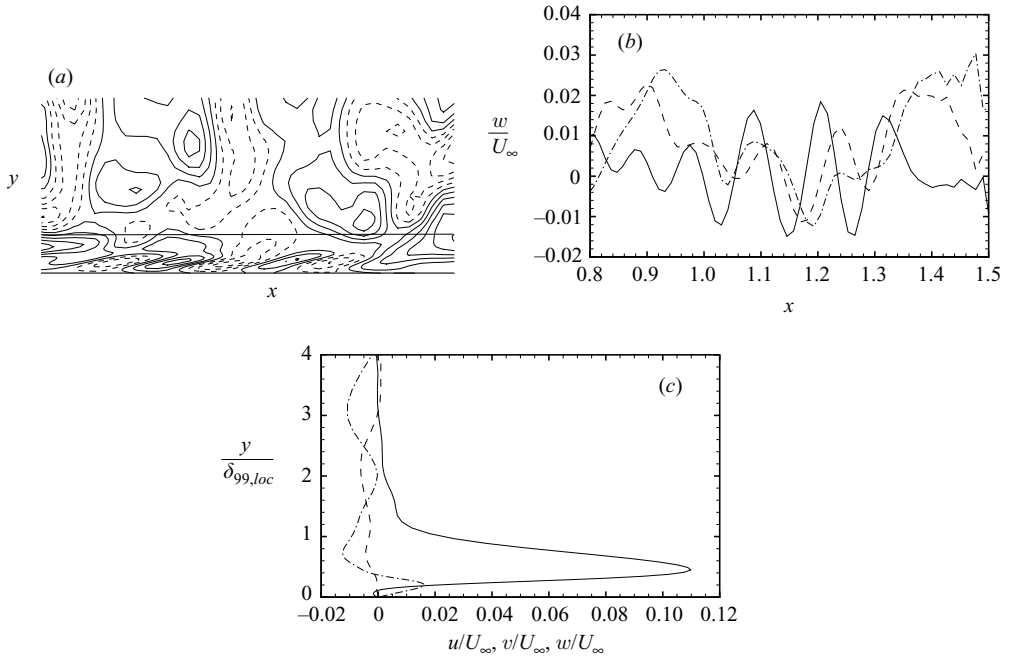


FIGURE 14. (*a*) Contours of spanwise velocity fluctuations in a spot precursor in the xy-plane. From case E with $-0.03 < w/U_\infty < 0.03$. Dashed lines: negative contours. y-coordinate is magnified by a factor of 2. (*b*) Spanwise velocity fluctuations versus streamwise coordinate in a spot precursor. ——, $y/\delta_{99,loc} = 0.25$; - - - -, $y/\delta_{99,loc} = 0.5$; —·—, $y/\delta_{99,loc} = 0.75$. (*c*) Wall-normal profiles of fluctuating velocity inside a spot precursor from case E. ——, u/U_∞; - - - -, v/U_∞; —·—, w/U_∞.

concentrated in the lower half of the boundary layer in a packet of fluid moving faster than the mean.

It should be noted that the wavepackets are analysed only after they have undergone considerable growth. Due to the presence of FST, it is hard to distinguish these wavepackets from the background non-uniformity in the buffeted boundary layer. It is only after sufficient growth in amplitude that these structures can be distinguished from the other disturbances that invariably exist in the boundary layer. Therefore, the initial stages of development of these wavepackets cannot be documented in detail. Furthermore, due to the presence of other disturbances, not all wavepackets appear as clean as the ones shown earlier. The main problem this poses is in the estimation of propagation rate of the leading and trailing edges of the wavepacket. Unlike the experiments of Gaster & Grant (1975) who studied wavepackets introduced into an otherwise laminar boundary layer, the leading and trailing edges of the wavepackets that appear in the present simulation are not well defined. In fact, as the amplitude decreases towards the leading and trailing edges, contamination from other sources dominates, and the signature of the wavepacket is lost.

A total of eight wavepackets from cases A, B and E were analysed. The dominant wavelength of a wavepacket is defined as the average distance between consecutive peaks and the average group velocity of a wavepacket is determined by measuring the distance the highest crest (or lowest trough) moves in a given small time interval. The dominant frequency is then evaluated using the wavelength and velocity so obtained

https://doi.org/10.1017/S0022112006001893 Published online by Cambridge University Press

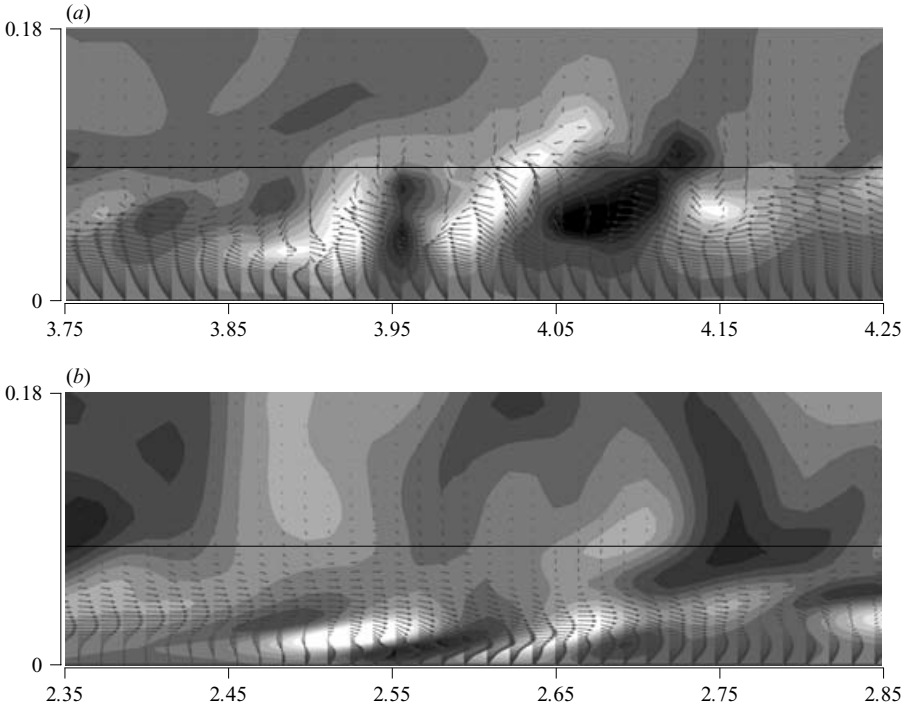


FIGURE 15. (*a*) Side-view (x, y-plane) of contours of spanwise velocity (levels: $-0.1 < w/U_\infty < 0.1$) and vectors of velocity fluctuation in plane. Early stages of the backward jet mechanism. (*b*) Side-view (x, y-plane) of contours of spanwise velocity (levels: $-0.06 < w/U_\infty < 0.06$) and vectors of velocity fluctuation in plane. A wavepacket-like spot precursor.

and renormalized using the standard form used to characterize TS waves:

$$F = \frac{\omega\nu}{U_\infty^2}.$$

It should to be pointed out that the frequency calculated from the wavelength and group velocity is only an approximate value and is not to be considered as exact. As a wavepacket consists of many wavelengths, with each moving at its own phase speed, the group velocity can be significantly different from the phase speed of an individual mode. However, at low values of Re_δ, the dispersion relation is close to linear (see Jordinson 1970) and therefore the group velocity can yield a fair approximation to the frequency. This procedure is used only to determine whether the disturbances are Tollmien-Schlichting waves.

The result of such a characterization process is presented in table 6, arranged in order of the distance from the leading edge where the wavepackets grow to large enough amplitudes to be discerned from the background fluctuations. Also indicated in the table is the simulation from which each spot is taken. The data indicate that spots that are seen further downstream have larger wavelength, and therefore lower frequency than those upstream. The speed at which individual crests or troughs travel varies from around $0.52U_\infty$ to $0.6U_\infty$ which is seen to be close to the speed at which the trailing edges of the wavepackets travel. On the other hand, the leading edges travel at somewhat higher speeds of around $0.7U_\infty$. Based on simple scaling

https://doi.org/10.1017/S0022112006001893 Published online by Cambridge University Press

Case	Wavelength λ	Speed u/U_∞	Frequency $F \times 10^6$	Distance x_{LE}
A	0.12	0.59	492	2.3
B	0.089	0.514	670	0.75
	0.086	0.528	714	0.8
	0.095	0.519	635	1.4
E	0.079	0.55	800	0.7
	0.086	0.56	757	0.75
	0.115	0.58	585	1
	0.135	0.56	481	1.05

TABLE 6. Summary of properties of wavepackets from cases A, B and E. x_{LE} is the distance from the leading edge where the wavepacket is first discerned.

using the wavelength in the wavepacket and its speed of travel, the frequency F is seen to lie in the range 500 to 800, much higher than typical frequencies of TS waves.

4.5. *A discussion of wavepackets in a boundary layer*

The wavepacket nature of the structures that lead to spot formation is reminiscent of natural transition through TS waves. Natural transition occurs when unstable TS waves grow (usually in a two-dimensional sense), modulate in the spanwise direction, and break down. Non-uniformity can cause TS waves to occur in the form of wavepackets that have been studied in controlled experiments by Gaster & Grant (1975) and analysed by Gaster (1968). The downstream development of the wavepacket in the experiments of Gaster & Grant (1975) occurred at group velocities in the TS range, with the leading and trailing edges of wavepackets travelling at speeds of $0.44U_\infty$ and $0.36U_\infty$ respectively. As the wavepacket evolves, it spreads in the spanwise direction. Eventually, certain oblique modes grow very rapidly and become large enough for nonlinearity to occur. Similar phenomena were observed by Cohen, Breuer & Haritonidis (1991) who tracked wavepackets from their inception, through linear growth and nonlinear evolution, to the eventual formation of turbulent spots. The dominant frequency in the wavepackets in this experiment corresponds to the most unstable one, which is around $\beta = \omega\delta^*/U_\infty \sim 0.1$ (Jordinson 1970; Drazin & Reid 1981). In terms of the frequency parameter F, at the conditions of the experiment, this translates into $F \times 10^6 \sim 80$. Further downstream, the peak shifts to the subharmonic at $\beta \sim 0.05$. The experimentally observed maximum frequency at which TS waves are unstable corresponds to $F \sim 400$. The wavepackets generated in experiments (Gaster & Grant 1975; Cohen *et al.* 1991) contain frequencies centred around the most unstable TS frequency. However, the wavepackets in the present simulations can contain only higher frequency unstable TS waves as they occur at Reynolds numbers close to branch I of the boundary layer stability boundary. At these Reynolds numbers, frequencies of growing disturbances lie in a narrow band around the frequency that becomes unstable at the critical Reynolds numbers. Furthermore, the boundary layer on the leading edge is subject to an adverse pressure gradient, causing the region of instability in the Reynolds number–frequency plane to be significantly larger (Wazzan 1975; Govindarajan & Narasimha 1995). For Falkner–Skan flows with adverse pressure gradients similar to those that exist in the leading-edge region, the range of unstable frequencies is much larger than for the Blasius boundary layers

https://doi.org/10.1017/S0022112006001893 Published online by Cambridge University Press

(see figure 14 in Wazzan 1975). In fact, for $m = -0.025$ (where m is the exponent in the Falkner–Skan velocity profile $U = Cx^m$), the maximum unstable frequency is twice that of a Blasius boundary layer. Therefore, higher unstable frequencies exist which may account for the observed higher frequencies in the spot precursors.

The wavepackets observed in the simulations travel at a mean speed of $0.52U_\infty$. Therefore, the leading- and trailing-edge speeds can be expected to be larger than those for the TS wavepackets. Furthermore, the frequency and speeds from the experiments of Cohen *et al.* (1991) indicate a dominant wavelength of $\lambda \sim 8\delta_{99,loc}$ while the wavelength in the simulations is around $\lambda \sim 5\delta_{99,loc}$. The higher speed and shorter wavelengths also translates into the higher frequencies observed in table 6 when compared to experiments. It can therefore be concluded that the spot precursors observed in the simulations are not TS wavepackets. It should be noted that the characteristics of the wavepackets excited in controlled experiments also show significant dependence on the level of excitation. At very small amplitudes, such as those in the experiments of Gaster & Grant (1975) and Cohen *et al.* (1991), the wavepacket leading and trailing edges travel at speeds of $0.44U_\infty$ and $0.36U_\infty$ respectively. On the other hand, as the level of excitation is increased, such as in the experiments of Vasudeva (1967), the leading- and trailing-edge speeds increases considerably to $0.8U_\infty$ and $0.6U_\infty$. Another experiment where high forcing was used is the study of incipient spots by Amini & Lespinard (1982) wherein the speeds were $0.95U_\infty$ and $0.5U_\infty$. This change in speed is probably due to the fact that a higher level of forcing in experiments (usually applied at the plate surface) is better able to excite waves at the outer edge of the boundary layer where the mean velocity is higher. The resulting wavepacket then moves with this higher speed. The wavepackets from the present simulations lie somewhere in between the weak and strongly forced experiments.

The stability of a nonlinearly saturated steady streak in a boundary layer was studied by Brandt *et al.* (2003) by observing the response of the streak to an impulsive force. The streak instability was shown to be convective in nature, with the resulting wavepacket moving with a trailing-edge velocity of $0.7U_\infty$. They concluded that their wavepacket, induced by spanwise shear further away from the wall than TS waves, is inviscid. While Brandt *et al.* (2003) noted their instability to be of the sinuous kind, there is an apparent symmetry of the leading-edge-induced wavepackets, as seen in figures 13(*a*), 13(*b*) and 13(*c*). Furthermore, it is clear that the wavepackets in our case are located much closer to the wall, and therefore move downstream at slower speeds, the trailing-edge convecting downstream at around $0.55U_\infty$.

TS wavepackets are only one of many kinds of localized disturbances that can occur in a boundary layer. Schmid & Henningson (2001) consider the growth of two other kinds of localized disturbances: axisymmetric jets and counter-rotating streamwise vortices. These were studied in detail by direct simulation and analysis for Poiseuille flow by Henningson, Lundbladh & Johansson (1993) and in zero- and adverse-pressure-gradient boundary layers by Bech, Henningson & Henkes (1998). In the study by Henningson *et al.* (1993), temporal simulations were conducted with a specified initial disturbance, and their subsequent evolution tracked. The contours of wall-normal velocity fluctuation in figure 14(*b*) appear qualitatively similar to those of an asymmetric small-amplitude streamwise vortex disturbance in Poiseuille flow (see figure 4 in Henningson *et al.* 1993). The asymmetry brings about spanwise shear that dominates the development of the disturbance. Compared to the symmetric case, Henningson *et al.* (1993) found that asymmetry increased transient growth considerably, which was attributed to generation of normal vorticity by normal

https://doi.org/10.1017/S0022112006001893 Published online by Cambridge University Press

velocity. This contribution to the disturbance kinetic energy was seen to dominate as the initial disturbance angle (relative to the streamwise axis) was increased. The wavepackets seen in the present simulations could be a manifestation of this process. However, the relevance of simulations for Poiseuille flow to a boundary layer is unclear. A similar initial value problem simulation for the Blasius boundary layer was carried out by Breuer & Landahl (1990), which was shown by Henningson *et al.* (1993) to suffer from under-resolution. Furthermore, the boundary layer simulations in Henningson *et al.* (1993) were at much higher Reynolds numbers, and therefore the difference between symmetric and asymmetric disturbances was not as pronounced as in Poiseuille flow.

Further simulations involving growth of localized disturbances in zero- and adverse-pressure-gradient boundary layers have been conducted by Bech *et al.* (1998). They study the linear and nonlinear evolution of three kinds of disturbances: a localized vortex pair, a wavepacket (not to be confused with what we call wavepackets in this study), and an axisymmetric disturbance in Blasius as well as Falkner–Skan boundary layers. They find that, in the initial stages, growth is dominated by the so-called *transient growth* mechanism leading to algebraic growth, whereas, at later times, the adverse pressure gradient case exhibits exponential growth. In the zero pressure gradient case, their wavepacket disturbance also exhibits exponential growth. However, their simulations were conducted at a Reynolds number of $Re_{\delta^*} = 950$, which allows the existence of growing TS waves. On the other hand, the disturbances observed in the present simulations occur at much lower Reynolds numbers where exponential growth due to amplification of TS waves is not possible (this does not imply that exponential growth is impossible, it may still occur due to secondary instabilities). Comparing figure 15(*b*) to the corresponding contour plots in Bech *et al.* (1998) shows qualitative similarity of our wavepackets with vortex-pair as well as axisymmetric disturbances. However, Bech *et al.* (1998) note that the axisymmetric disturbance is slower to transition. On the other hand, the initial disturbance containing a vortex pair underwent early breakdown when the initial amplitude was large enough. Given the similarities of the present transition process with that of Bech *et al.* (1998), we can expect the transition induced by the leading edge to follow a similar path, a possibility that is investigated further in § 5.1 with pairs of free-stream vortices that interact with the boundary layer.

5. Origin of precursors to turbulent spots

As demonstrated thus far, the same inflow turbulence field leads to different paths to transition in cases A and E. As the only difference between the two cases is the geometry of the leading edge, it is reasonable to expect the change in transition location to be a direct consequence of this difference. Numerical simulations provide the ability to track flows back in time and identify the cause of the phenomenon under investigation. Using snapshots of the flow field, the wavepackets are tracked backwards to their antecedents. Quantitative measures such as the time of travel along mean streamlines were found to be very sensitive to the choice of the streamline due to the large velocity gradients around the leading edge and inside the boundary layer. Tracking of wavepackets visually using a sequence of snapshots was found to be the most reliable method. One wavepacket from case E is traced back to the leading edge in figures 16(*a*) and 16(*b*). The first snapshot shows the wavepacket in its final form and the second shows a snapshot at an earlier time when the wavepacket is spawned. An analysis of many such wavepackets show that almost all of them are created when

https://doi.org/10.1017/S0022112006001893 Published online by Cambridge University Press

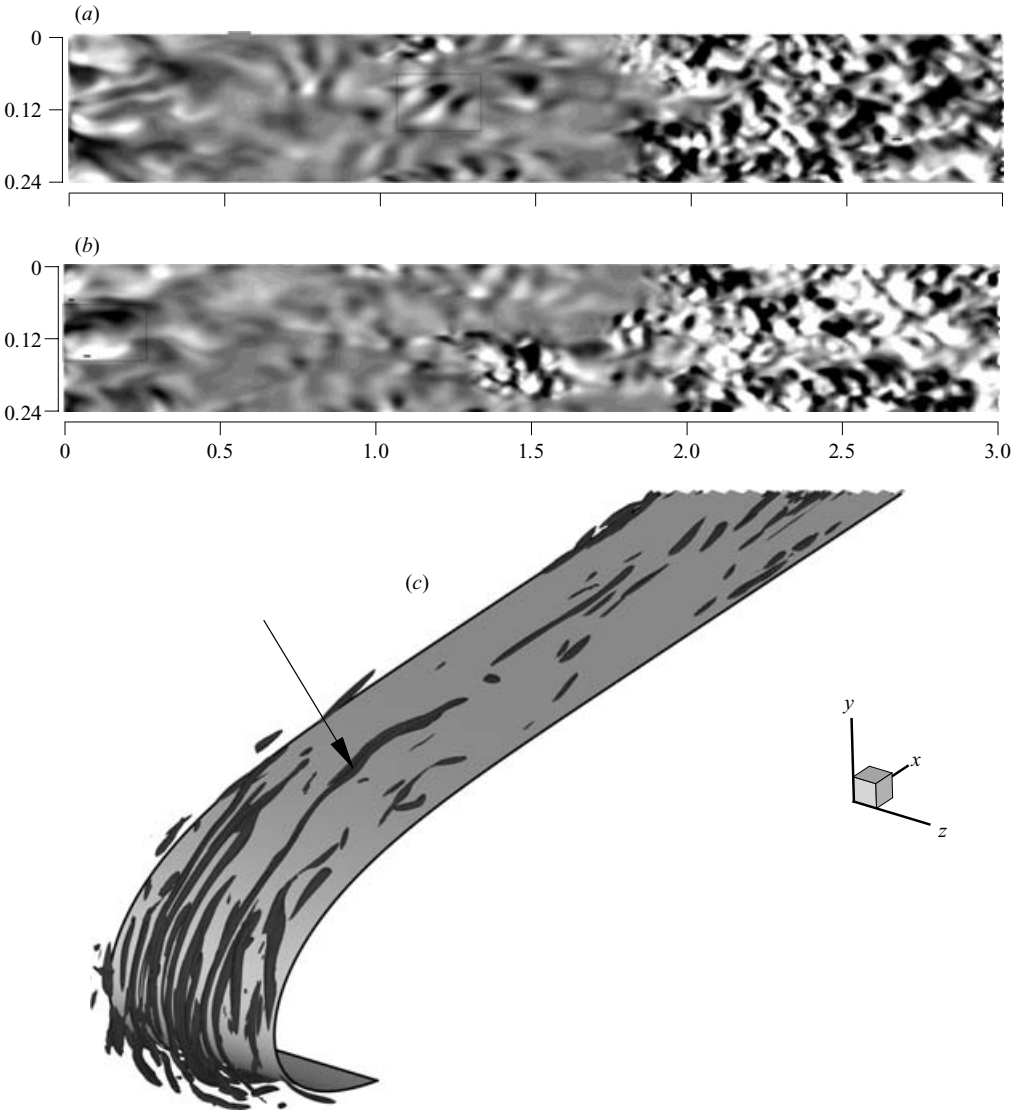


FIGURE 16. (*a*) A spot precursor from case E. (*b*) Antecedent, at the leading edge, of the structure in (*a*). (*c*) Antecedent to a spot precursor traced back to vortices at the leading edge, identified by iso-surfaces of λ_2. Vortices shown at the time instant corresponding to the snapshot in (*b*). Arrow indicates the vortex responsible for inducing the antecedent.

strong spanwise flow occurs in the leading-edge region. A visualization of the vortex tubes (identified using the λ_2 method of Jeong & Hussain 1995) in figure 16(*c*) in the leading-edge region also shows a strong vortex wrapped around the leading edge at the spanwise location of the wavepacket.

Almost all of the wavepackets were formed when a particularly energetic vortex is extended downstream of the stagnation plane by virtue of being wrapped around the leading edge. At the low turbulence level and sharp leading edge of case A, such vortices and the associated spanwise shear were few and far between. Hence the rarity of spots formed through wavepackets. On the other hand, with higher turbulence

https://doi.org/10.1017/S0022112006001893 Published online by Cambridge University Press

intensity (or blunter leading edge), such strong vortices occur more frequently and thus are able to affect transition through the higher rate of production of the wavepackets that lead to spot formation. However, not all wavepackets that are spawned at the leading edge lead to the formation of a spot. Some exhibit transient growth followed by decay. Such precursors, though they become large enough to be seen in the boundary layer, do not produce any turbulent spots.

5.1. *Formation of wavepackets*

Simulations with localized vortices introduced into the domain from the inflow boundary confirm the formation of spot precursors at the leading edge by wrapped vortices. Furthermore, such 'clean' simulations shed more light on the mechanism that leads to the formation of the wavepackets. A pair of counter-rotating vortices (Taylor 1918), aligned along the y-axis, centred about the plane $z = 0.12$, are imposed at the inflow boundary using

$$u_\theta = \frac{\mathscr{M} r}{16\pi\nu^2 t^2} \exp\left(-\frac{r^2}{r_c^2}\right) \tag{5.1}$$

where t and r are time and distance from the centre of the vortex respectively, ν is the coefficient of kinematic viscosity, $\mathscr{M}$ is the total angular momentum of the vortex, given by

$$\mathscr{M} = \int_0^\infty u_\theta r \; 2\pi r \, \mathrm{d}r \tag{5.2}$$

and $r_c = \sqrt{4\nu t}$ is a representative size of the vortex, which we call the core radius. The vortex strength is chosen so that the maximum value of the tangential velocity is $u_\theta \sim 0.02 U_\infty$ and the core radius is $2\delta_{99}$ at the junction of the plate and the leading edge.

The vortices convect downstream, are stretched around the leading edge, and interact with the boundary layer. The difference between these simulations and those of Bech *et al.* (1998) is in the receptivity process. While Bech *et al.* (1998) start with initial conditions wherein disturbances are already inside the boundary layer, the current simulation uses vortices that are outside. Therefore, the receptivity process by which these free-stream disturbances enter the boundary layer is also included. Figures 17(*a*), 17(*b*) and 17(*c*) show the plan-view of velocity fluctuations in the boundary layer (at $y/\delta_{99,loc} \sim 0.25$) and the associated streamwise profiles of spanwise velocity are shown in figure 17(*d*). These velocity contours are qualitatively similar to those in figures 15(*a*), 15(*b*) and 15(*c*). The symmetry of the response about the $z = 0.12$ plane is a consequence of the symmetry of the disturbance. However, such a symmetry, about the precursor centre plane, is also evident in the spot precursors. This is manifested in the form of a change in sign of the spanwise velocity while the streamwise and wall-normal velocities do not change sign. The spanwise profiles in figure 17(*d*) show the localized disturbance left behind by the vortex pair, which has moved out of the frame. The spot precursor of figure 13(*d*) has a similar structure. Further similarity is evident in the side view of the disturbance inside the boundary layer, shown in figure 18(*a*), whose inclined shear layers are similar to those of the spot precursor of figure 14(*a*). However, it should be noted that the disturbances in the spot precursor are located lower in the boundary layer than those in the Taylor's vortex case. Streamwise profiles of the spanwise velocity shown in figure 18(*b*) at different wall-normal locations are also similar to those of figure 14(*b*). The maximum disturbance velocity occurs in the lower half of the boundary layer at $y \sim \delta_{99,loc}/4$.

https://doi.org/10.1017/S0022112006001893 Published online by Cambridge University Press

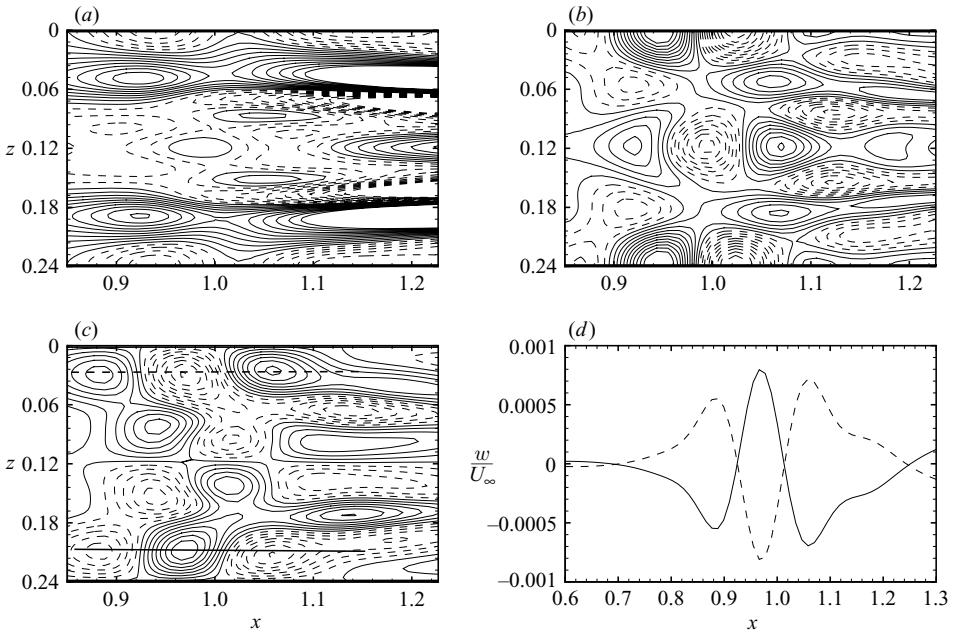


FIGURE 17. Plan view of response of the boundary layer to a pair of counter-rotating Taylor's vortices. Shown are (*a*) *u*-, (*b*) *v*- and (*c*) *w*-velocity contours at $y = \delta_{99,loc}/4$. (*d*) Spanwise velocity fluctuation versus streamwise coordinate along lines —— and —— drawn in (*c*).

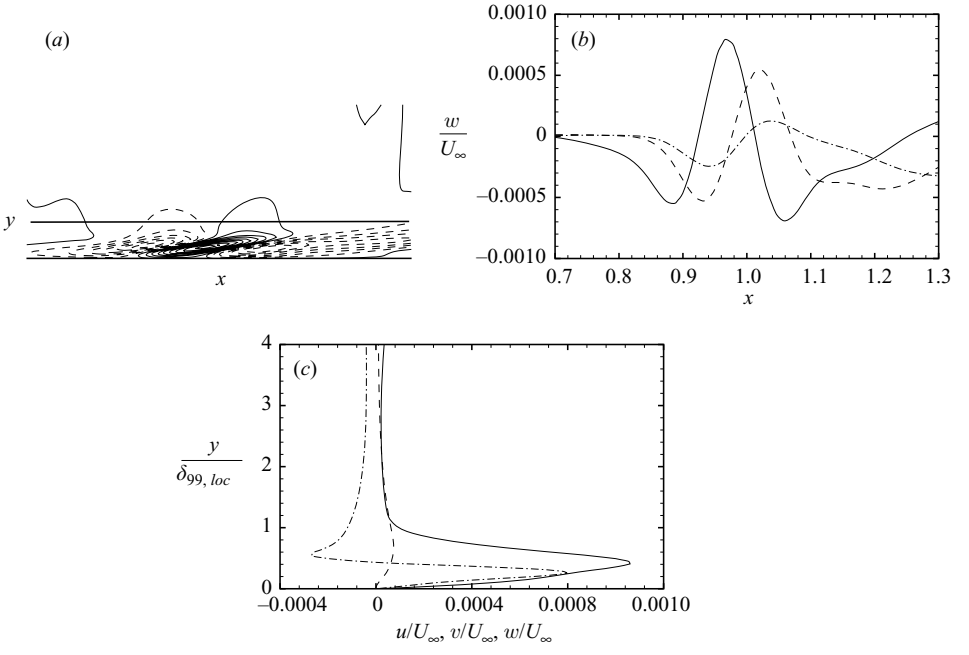


FIGURE 18. (*a*) Contours of spanwise velocity fluctuations in the boundary layer in the (x, y)-plane. From Taylor vortex case with $-2 \times 10^{-3} < w/U_\infty < 2 \times 10^{-3}$. Dashed lines: negative contours. *y*-coordinate is magnified by a factor of 2. (*b*) Spanwise velocity fluctuations versus streamwise coordinate. ——, $y/\delta_{99,loc} = 0.25$; - - - -, $y/\delta_{99,loc} = 0.5$; —·—, $y/\delta_{99,loc} = 0.75$. (*c*) Wall-normal profiles of fluctuating velocity in the boundary layer. ——, u/U_∞; - - - -, v/U_∞; —·—, w/U_∞.

https://doi.org/10.1017/S0022112006001893 Published online by Cambridge University Press

The wall-normal profiles of velocity disturbances in the boundary layer are shown in figure 18(*c*). The peak spanwise velocity occurs at $y/\delta_{99,loc} \sim 0.25$ as in figure 14(*c*).

The speed of the wavepacket left behind by the interaction of the vortices with the leading edge and the boundary layer is evaluated by measuring its streamwise location at various times. For the vortices used in this study, the average speed is $\sim 0.5U_\infty$. Simulations with vortices of larger core radii indicate that this speed is insensitive to the size of the vortex and its ability to penetrate the boundary layer. However, all the vortices considered cause small responses that are decaying in time. This is evident from figure 18(*b*) where the maximum amplitude of the spanwise velocity in the boundary layer is around $w/U_\infty \sim 0.002$, and decreases as the disturbance convects downstream.

The similarities between the response of the boundary layer vortices aligned normal to the wall and free-stream turbulence leads us to believe that the interaction of such vortices with the leading edge results in the formation of spot precursors. The resultant disturbance inside the boundary layer is in the form of localized streamwise vorticity, also studied by Breuer & Landahl (1990), Breuer & Haritonidis (1990), Henningson *et al.* (1993), and Bech *et al.* (1998). However, we have so far been unable to determine the conditions under which free-stream vortices lead to growing localized disturbances inside the boundary layer as seen by Bech *et al.* (1998). This remains a topic for further research.

6. Discussion

In this section, we consider some of the earlier efforts to study the effects of leading edges on bypass transition and our observations are compared to theirs. While comparisons cannot be direct as the conditions of the previous experiments and theoretical treatments are different from our simulations, some useful information can be gleaned through qualitative comparisons.

Careful experiments were conducted by Kendall (1991) to study the effect of leading-edge bluntness on the response of a flat-plate boundary layer forced by low levels of free-stream turbulence ($u_{rms}/U_\infty < 0.4\,\%$). Watmuff (1997) also conducted similar experiments aimed at minimizing the amplitude of Klebanoff modes in the boundary layer in a tunnel where the maximum free-stream turbulence intensity was 0.12 %. Both experiments demonstrate the insensitivity of Klebanoff modes to leading-edge bluntness and shape. On the other hand, Kendall (1991) observed the TS wave response in the boundary layer to increase nonlinearly with bluntness. However, in the present computations, using two different methods for TS wave detection, i.e. (i) a differential pressure measurement as used by Kendall (1991) and (ii) a decomposition of the disturbances into an expansion in terms of the eigenfunctions (Grosch & Salwen 1981) and evaluating the magnitude of the coefficient of the TS eigenfunction of interest, revealed that the energy contained in the TS waves is insignificant. This is possibly because the TS waves are overwhelmed by other disturbances (such as the wavepacket-like spot precursors) induced by free-stream turbulence which is much stronger in the simulations than the experiments of Kendall (1991), which are much lower than the threshold above which bypass mechanisms, let alone leading edge effects, dominate. Therefore, while the leading edge may have a larger influence on the amplitude of TS waves, other mechanisms, including anisotropy and leading-edge-induced disturbances dominate at higher turbulence levels.

The model used in the experiments conducted by Westin *et al.* (1994) (and in later studies such as that of Matsubara & Alfredsson 2001) was designed using potential

https://doi.org/10.1017/S0022112006001893 Published online by Cambridge University Press

flow simulations to remove the suction peak on the working surface of the plate. In spite of this careful design, a significant upstream shift of transition was observed when the suction peak was only about 10 % of the dynamic pressure. A similar trend can be seen from the present simulations where, for the same free-stream conditions, the leading edge with the larger suction peak (case E with the blunter leading edge) shows earlier transitiion (compared to case A).

As already discussed, Goldstein & Wundrow (1998) argue that the stretching of vortices around the leading edge leads to streamwise vortices, which then induce streamswise velocity perturbations of the Klebanoff mode type. In subsequent work, Wundrow & Goldstein (2001) show that streamwise vortices are indeed effective in producing Klebanoff modes as well as, in the nonlinear region downstream, low-speed streaks as seen in simulations. However, this hypothesis assumes that transition with and without leading-edge effects occurs by the same mechanism. The leading edge simply causes it to happen sooner by enhancing the growth of Klebanoff modes by vortex stretching. The present simulations show that there is a far stronger effect, also due to vortex stretching, of localized regions of streamwise vorticity in the boundary layer that grow and breakdown quickly. Growth of these disturbances is augmented by the adverse-pressure-gradient region over the leading edge (Bech *et al.* 1998). Furthermore, growth rate can also be higher as they evolve in a buffeted boundary layer where near-wall inflection points are present.

7. Conclusions

Simulations of bypass transition of a boundary layer on a flat plate with a blunt leading edge have been carried out. The leading-edge aspect ratio as well as the free-stream turbulence characteristics are varied to cover a wide range of parameters and to elucidate the effect of various parameters on transition onset and length. The results indicate that when the leading edge is sharp, and the free-stream turbulence weak, transition occurs through instabilities developing on low-speed streaks as in the simulations of Brandt *et al.* (2004). This mechanism is the same as the one described by Jacobs & Durbin (2001) as interaction of high-frequency free-stream eddies with backward jets. The well-established dependence of bypass transition on turbulence intensity and length scale have also been confirmed, i.e. transition moves upstream with increase in intensity as well as turbulence integral scale. On the other hand, for a given leading edge, when the turbulence intensity or the length scale exceeds a certain threshold, transition occurs through growth and breakdown of wavepacket-like disturbances in the boundary layer and not through the sinuous instability mechanism. The transition scenario that emerges from this study is as follows: vortex stretching around the leading edge induces localized streamwise vorticity in the boundary layer. These disturbances grow as they convect downstream, their growth rate being higher in the adverse-pressure-gradient region (Bech *et al.* 1998). After linear and nonlinear growth, breakdown to turbulence occurs. Growth could be further augmented by inflectional velocity profiles close to the wall. Simulations of the boundary layer interacting with a pair of counter-rotating vortices shows a response qualitatively similar to the spot precursor. Therefore, at similar free-stream turbulence characteristics, a blunter leading edge is seen to lead to earlier onset of transition.

This work was supported by the ASC program of the US Department of Energy. The authors would also like to thank an anonymous referee for bringing to our attention the relevant paper by Bech *et al.* (1998).

https://doi.org/10.1017/S0022112006001893 Published online by Cambridge University Press

REFERENCES

Abu-Ghannam, B. J. & Shaw, R. 1980 Natural transition of boundary layers – the effects of turbulence, pressure gradient, and flow history. *J. Mech. Engng Sci.* **22** (5), 213–228.

Amini, J. & Lespinard, G. 1982 Experimental study of an 'incipient spot' in a transitional boundary layer. *Phys. Fluids* **25**, 1743–1750.

Andersson, P., Berggren, M. & Henningson, D. S. 1999 Optimal disturbances and bypass transition in boundary layers. *Phys. Fluids* **11**, 134–150.

Andersson, P., Brandt, L., Bottaro, A. & Henningson, D. S. 2001 On the breakdown of boundary layer streaks. *J. Fluid Mech.* **428**, 29–60.

Aris, R. 1989 *Vectors, Tensors, and the Basic Equations of Fluid Mechanics*. Dover.

Bech, K. H., Henningson, D. S. & Henkes, R. A. W. M. 1998 Linear and nonlinear development of localized disturbances in zero and adverse pressure gradient boundary layers. *Phys. Fluids* **10**, 1405–1418.

Benney, D. J. & Gustavsson, L. H. 1981 A new mechanism for linear and nonlinear hydrodynamic instability. *Stud. Appl. Math.* **64**, 185–209.

Brandt, L., Cossu, C., Chomaz, J.-M., Huerre, P. & Henningson, D. S. 2003 On the convectively unstable nature of optimal streaks in boundary layers. *J. Fluid Mech.* **485**, 221–242.

Brandt, L. & Henningson, D. S. 2002 Transition of streamwise streaks in zero-pressure-gradient boundary layers. *J. Fluid Mech.* **472**, 229–261.

Brandt, L., Schlatter, P. & Henningson, D. S. 2004 Transition in boundary layers subject to free-stream turbulence. *J. Fluid Mech.* **517**, 167–198.

Breuer, K. S. & Haritonidis, J. H. 1990 The evolution of a localized disturbance in a laminar boundary layer. Part 2. Weak disturbances. *J. Fluid Mech.* **220**, 569–594.

Breuer, K. S. & Landahl, M. T. 1990 The evolution of a localized disturbance in a laminar boundary layer. Part 2. Strong disturbances. *J. Fluid Mech.* **220**, 595–621.

Butler, K. M. & Farrell, B. F. 1992 Three-dimensional optimal perturbations in viscous flow. *Phys. Fluids* **4**, 1637–1650.

Cohen, J., Breuer, K. S. & Haritonidis, J. H. 1991 On the evolution of a wavepacket in a laminar boundary layer. *J. Fluid Mech.* **225**, 575–606.

Collis, S. S. 1997 A computational investigation of receptivity in high-speed flow near a swept leading-edge. PhD thesis, Stanford University.

Crow, S. C. 1966 The spanwise perturbation of two-dimensional boundary layers. *J. Fluid Mech.* **24**, 153–164.

Drazin, P. G. & Reid, W. H. 1981 *Hydrodynamic Stability*. Cambridge University Press.

Dryden, H. L. 1936 Airflow in the boundary layer near a plate. *NACA Rep.* 562. National Advisory Committee for Aeronautics.

Gaster, M. 1968 The development of three-dimensional wavepackets in a boundary layer. *J. Fluid Mech.* **32**, 173–184.

Gaster, M. & Grant, I. 1975 An experimental investigation of the formation and development of a wave packet in a laminar boundary layer. *Proc. R. Soc. Lond.* **347**, 253–269.

Giles, M. B. 1990 Nonreflecting boundary conditions for Euler equation calculations. *AIAA J.* **28**, 2050–2058.

Goldstein, M. E. & Wundrow, D. W. 1998 On the environmental realizability of algebraically growing disturbances and their relation to Klebanoff modes. *Theor. Comput. Fluid Dyn.* **10**, 171–186.

Govindarajan, R. & Narasimha, R. 1995 Stability of spatially developing boundary layers in pressure gradients. *J. Fluid Mech.* **300**, 117–147.

Grosch, C. E. & Salwen, H. 1981 The continuous spectrum of the Orr-Sommerfeld equation. Part 2. Eigenfunction expansions. *J. Fluid Mech.* **104**, 445–465.

Henningson, D. S., Lundbladh, A. & Johansson, A. V. 1993 A mechanism for bypass transition from localized disturbances in wall-bounded shear flows. *J. Fluid Mech.* **250**, 169–207.

Hultgren, L. S. & Gustavsson, L. H. 1981 Algebraic growth of disturbances in a laminar boundary layer. *Phys. Fluids* **104**, 1000–1004.

Hunt, J. C. R. & Durbin, P. A. 1999 Perturbed vortical layers and shear sheltering. *Fluid Dyn. Res.* **24**, 375–404.

https://doi.org/10.1017/S0022112006001893 Published online by Cambridge University Press

Jacobs, R. G. & Durbin, P. A. 1998 Shear sheltering and the continuous spectrum of the Orr-Sommerfeld equation. *Phys. Fluids* **10**, 2006–2011.

Jacobs, R. G. & Durbin, P. A. 2001 Simulations of bypass transition. *J. Fluid Mech.* **428**, 185–212.

Jeong, J. & Hussain, F. 1995 On the identification of a vortex. *J. Fluid Mech.* **285**, 69–94.

Johnson, M. W. & Ercan, A. H. 1999 A physical model for bypass transition. *Intl J. Heat Fluid Flow* **20**, 95–104.

Jonas, P., Mazur, O. & Uruba, V. 2000 On the receptivity of the by-pass transition to the length scale of the outer stream turbulence. *Eur. J. Mech.* B *Fluids* **19**, 707–722.

Jordinson, R. 1970 The flat plate boundary layer. Part 1. Numerical integration of the Orr-Sommerfeld equation. *J. Fluid Mech.* **43**, 801–811.

Kendall, J. M. 1985 Experimental study of disturbances produced in a pre-transitional boundary layer by weak free-stream turbulence. *AIAA Paper* 85-1695.

Kendall, J. M. 1991 Studies on laminar boundary-layer receptivity to freestream turbulence near a leading edge. In *Boundary Layer Stability and Transition to Turbulence* (ed. D. C. Reda, H. L. Reed & R. Kobayashi), pp. 23–30. ASME.

Kendall, J. M. 1998 Experiments on boundary-layer receptivity to freestream turbulence. *AIAA Paper* 98-0530.

Klebanoff, P. S., Tidstrom, K. D. & Sargent, L. M. 1962 The three-dimensional nature of boundary-layer instability. *J. Fluid Mech.* **12**, 1–24.

Klingmann, B. G. B., Boiko, A. V., Westin, K. J. A., Kozlov, V. V. & Alfredsson, P. H. 1993 Experiments on the stability of Tollmien-Schlichting waves. *Eur. J. Mech.* B *Fluids* **12**, 493–514.

Leib, S. J., Wundrow, D. W. & Goldstein, M. E. 1999 Effect of free-stream turbulence and other vortical disturbances on a laminar boundary layer. *J. Fluid Mech.* **380**, 169–203.

Luchini, P. 2000 Reynolds-number-independent instability of the boundary layer over a flat surface: optimal perturbations. *J. Fluid Mech.* **404**, 289–309.

Matsubara, M. & Alfredsson, P. H. 2001 Disturbance growth in boundary layers subjected to free-stream turbulence. *J. Fluid Mech.* **430**, 149–168.

Mohamed, M. S. & LaRue, J. C. 1990 The decay power law in grid-generated turbulence. *J. Fluid Mech.* **219**, 195–214.

Morkovin, M. V. 1969 The many faces of transition. In *Viscous Drag Reduction* (ed. C. S. Wells). Plenum Press.

Nagarajan, S., Lele, S. K. & Ferziger, J. H. 2003 A robust high-order method for large eddy simulation. *J. Comput. Phys.* **191**, 392–419.

Nagarajan, S., Lele, S. K. & Ferziger, J. H. 2004 A high-order method for mixed direct and large-eddy simulation of turbulent and transitional flows. *In preparation*.

Reddy, S. C. & Henningson, D. S. 1993 Energy growth in viscous channel flows. *J. Fluid Mech.* **252**, 209–238.

Roach, P. E. & Brierley, D. H. 1992 The influence of a turbulent free-stream on zero pressure gradient transitional boundary layer development Part 1: Test cases T3A and T3B. In *Numerical Simulation of Unsteady Flows and Transition to Turbulence* (ed. O. Pironneau, W. Rodi & I. L. Ryhming), pp. 319–347. Cambridge University Press.

Schmid, P. J. & Henningson, D. J. 2001 *Stability and Transition in Shear Flows*. Springer.

Taylor, G. I. 1918 On the dissipation of eddies. *R&M* 598. British Aeronautical Research Committee.

Taylor, G. I. 1939 Some recent developments in the study of turbulence. In *Proc. Fifth Intl Congress for Applied Mathematics* (ed. J. P. D. Hartog & H. Peters), pp. 294–310. Wiley.

Trefethen, L. N., Trefethen, A. E., Reddy, S. C. & Driscoll, T. A. 1993 Hydrodynamic stability without eigenvalues. *Science* **261**, 578.

Vasudeva, B. R. 1967 Boundary-layer instability experiment with localized disturbance. *J. Fluid Mech.* **29**, 745–763.

Watmuff, J. 1997 Detrimental effects of almost immeasurably small free-stream nonuniformities generated by wind tunnel screens. *AIAA Paper* 97-0228.

Wazzan, A. R. 1975 Spatial stability of tollmien-schlichting waves. *Prog. Aerospace Sci.* **16**, 99–127.

Westin, K. J. A., Boiko, A. V., Klingmann, B. G. B., Kozlov, V. V. & Alfredsson, P. H. 1994 Experiments in a boundary layer subjected to free stream turbulence. Part 1. Boundary layer structure and receptivity. *J. Fluid Mech.* **281**, 193–218.

https://doi.org/10.1017/S0022112006001893 Published online by Cambridge University Press

White, F. M. 1991 *Viscous Fluid Flow*. McGraw-Hill.

Wundrow, D. W. & Goldstein, M. E. 2001 Effect on a laminar boundary layer of small-amplitude streamwise vorticity in the upstream flow. *J. Fluid Mech.* **426**, 229–262.

Xiong, Z. 2004 Stagnation point flow and heat transfer under free-stream turbulence. PhD thesis, Stanford University.

Xiong, Z., Nagarajan, S. & Lele, S. K. 2004 A simple method for generating inflow turbulence. *AIAA J.* **42**, 2164–2166.

Zaki, T. A. & Durbin, P. A. 2005 Mode interaction and the bypass route to transition. *J. Fluid Mech.* **531**, 85–111.

https://doi.org/10.1017/S0022112006001893 Published online by Cambridge University Press